Euro-Mediterranean Journal for Environmental Integration (2024) 9:235–254
https://doi.org/10.1007/s41207-023-00442-7

ORIGINAL PAPER

Hamama volcanogenic massive sulfide deposits, central Eastern Desert, Egypt: mineralogical and tectonic implications

Abdel-Aal M. Abdel-Karim[1] · Shehata Ali[2] · Adel H. El-Afandy[3] · Amr El-Awady[1] · Mohamed Z. Khedr[4] · Akihiro Tamura[5] · Waheed Elwan[1]

Received: 8 February 2023 / Accepted: 11 November 2023 / Published online: 29 December 2023

Abstract

The Hamama metavolcanics and their sulfide deposits are an important part of the Neoproterozoic Shadli bimodal metavolcanics in the central Eastern Desert (CED) of Egypt and recently became a promising target for gold exploration in Egypt. Semi-massive to massive sulfide deposits occur in quartz-carbonate exhalite and as disseminated grains in metabasalt and metadacite. The Hamama prospect comprises polymetallic bimodal-mafic-type volcanogenic massive sulfide (VMS) deposits, particularly Zn–Cu–Ag–Au VMS deposits. Polybasite is a silver-bearing sulfosalt (65.17–71.81 wt% Ag). Arsenic-bearing framboidal pyrite is the main host of the precious metals (Au and Ag contents reach up to 0.12 wt% and up to 0.55 wt%, respectively). The arsenic-rich fluids likely promoted gold and silver accumulation in framboidal pyrite, which is hosted in the quartz-carbonate exhalite. This exhalite may have acted as a cap rock preventing the dissipation of the metal-rich hydrothermal fluids. Gold- and silver-bearing sulfides were possibly formed in a back-arc basin, which is considered as a suitable environment for VMS formation. The dominance of Zn and Ag reveals that the Hamama VMS deposits were generated at low temperature and a shallow water depth during rifting of the intra-oceanic island arc. Supergene processes formed secondary copper deposits in the upper part of the exhalite. Gold and silver are also accumulated in the gossan zone that is formed by low-temperature oxidized fluids. The factors controlling precious metal mineralization in the CED of Egypt are possibly related to the composition of the host rock and the hydrothermal fluid beside shear zones that act as channels for fluid circulation in an extensional tectonic setting.

Keywords Precious metals · Quartz-carbonate exhalite · Gossan zone · Neoproterozoic Shadli metavolcanics · Intra-arc rifting

Introduction

Volcanogenic massive sulfide (VMS) deposits are usually polymetallic (e.g., Zn-Pb-Cu-Au–Ag) massive sulfide lenses formed at or near the seafloor due to the circulation of metal-bearing hydrothermal fluids in the subsurface (Large 1992; Franklin et al. 2005; Galley et al. 2007; Piercey et al. 2014; Abd El-Rahman et al. 2015). Hydrothermal fluids arise from a volcanic vent and combine with seawater, causing the deposition of sulfides on the seafloor as exhalative deposits (Ohmoto 1996; Franklin et al. 2005). VMS deposits are generally hosted by volcanic, volcano-sedimentary, and sedimentary rocks (Large 1992; Barrie and Hannington 1999; Galley et al. 2007; Abd El-Rahman et al. 2015). They represent an essential source of base (Cu, Zn, Pb) and precious (Au, Ag) metals (Singer 1995; Galley et al. 2007; Abd El-Rahman et al. 2015) and are formed by different genetic

Responsible Editor: Settimio Ferlisi.

This paper belongs to the special issue The 11th International Conference on the Geology of Africa "ICGA-11".

✉ Shehata Ali
shehata.ali@mu.edu.eg

[1] Geology Department, Faculty of Science, Zagazig University, Zagazig 44519, Egypt

[2] Geology Department, Faculty of Science, Minia University, El-Minia 61519, Egypt

[3] Nuclear Materials Authority, El Maadi, Cairo, Egypt

[4] Department of Geology, Kafrelsheikh University, Kafrelsheikh, Egypt

[5] Department of Earth Sciences, Kanazawa University, Kakuma, Kanazawa 920-1192, Japan

processes (e.g., Hannington et al. 1999). These deposits are generally associated with arc and ophiolite assemblages that were formed mainly in rifted back-arc or marginal basins (Franklin et al. 2005; Piercey 2011; Khedr et al. 2023). VMS deposits were formed over geologic time in extensional geodynamic settings and during accretionary orogenesis (e.g., Huston et al. 2010; Piercey 2011; Hannington 2014). They are grouped according to their base metal contents into Cu–Zn, Zn–Cu, and Zn–Pb–Cu groups (Large 1992). Moreover, they are classified into normal and Au-rich VMS deposits according to their gold contents (Poulsen and Hannington 1995).

The Arabian-Nubian Shield (ANS) was formed due to the accretion of island arcs and microcontinents (850−620 Ma) during the terminal collision between East and West Gondwana (Stern 1994; Fritz et al. 2013). Several volcanogenic base metal deposits in the ANS have been documented (e.g., Al-Shanti et al. 1993; Barrie et al. 2007; Surour and Bakhsh 2013; Harbi et al. 2014; Abd El-Rahman et al. 2015; Khedr et al. 2023). The Neoproterozoic Shadli metavolcanics, a part of the ANS, represent one of the most important rock units in the basement complex of the Eastern Desert of Egypt because they host volcanogenic Zn–Cu deposits with precious metals (Minex Mineral Egypt 1991; Aton 2012). They are bimodal island-arc assemblages consisting of weakly metamorphosed mafic and felsic rocks (Abd El-Rahman et al. 2015; Abdel-Karim et al. 2019; Khedr et al. 2023). These rock assemblages are relatively scarce in the northern Eastern Desert (NED) but present large exposures in the central (CED) and southern (SED) parts of the Eastern Desert of Egypt (El-Gaby 1994; Khedr et al. 2023). The volcanogenic base metal deposits occur in the Eastern Desert in the vicinity of the Um Samiuki area, which is possibly the main VMS deposit in Egypt (e.g., Takla et al. 1998; Helmy 1999; Botros 2003; Shalaby et al. 2004).

The Hamama area, one of the best outcrops of the Shadli metavolcanics, is located near the major NE–SW-trending shear zone in the CED of Egypt (Fig. 1). El-Gaby et al. (1988) described this shear as a major dextral strike-slip shear zone. It is also considered as a major steep extensional shear zone (Fowler et al. 2006) and as a low-angle thrust fault overprinted by strike-slip shear zones with complex orientations (Kamal El-Din and Abdelkareem 2018).

Few studies have been carried out on the geology, petrography, and mineralization of the Hamama area (Abdel Nabi et al. 1977). Abd El-Rahman et al. (2015) stated that the Hamama sulfide deposits were mainly hosted by tholeiitic bimodal volcanic rocks with island-arc geochemical signatures. These deposits exhibit geologic features (i.e., ore body geometries, metal grades, and mineral alteration) comparable to other major VMS deposits in the ANS (Barrie et al. 2007; Aton 2012). Abdel-Karim et al. (2019) studied the petrography, the mineral chemistry of silicates, and the geochemistry of the Hamama metavolcanics. They concluded that the Hamama metavolcanics were derived from arc-related magmas at a subduction zone setting.

This study presents new field geology, petrography, and mineral chemistry data for the sulfide deposits hosted in the Hamama metavolcanics and the quartz-carbonate horizon. Moreover, new trace and rare earth elements (REEs) in the clinopyroxene (Cpx) of basalts are presented to provide information about the mantle source and tectonic setting of these basalts.

The main objective of this study was to understand the origin of these deposits and the genetic relationship of these deposits with their host rocks and to discuss their tectonic setting and mode of deposition. In addition, data from Aton (2012, 2017) are used to obtain a better understanding of the origin of the Hamama VMS deposits.

Geologic setting

Regional geologic setting

The Precambrian basement rocks of the Egyptian Nubian Shield, a part of the ANS, consist of volcano-sedimentary sequences, ophiolite assemblages, a metagabbro/diorite complex, and calc-alkaline granites that were formed during the island-arc phase (Kröner et al. 1994; Abdelsalam and Stern 1996; Stern 2002; Johnson et al. 2011; Abdel-Karim et al. 2016, 2018; El-Bialy 2020; Ali et al. 2021, 2023; Sami et al. 2023). The syntectonic granites in the Eastern Desert of Egypt are younger than 750 Ma and are I-type granites that were formed during active subduction processes (Stern and Hedge 1985; El-Gaby et al. 1990; Kröner et al. 1994; Farahat et al. 2007; Ali et al. 2016; Sami et al. 2023). Moreover, the undeformed late-collisional highly evolved calc-alkaline granites were formed after the crustal thickening stage and before the beginning of the crustal extension period (630–590 Ma) (Stern and Hedge 1985; El-Gaby et al. 1990; Kröner et al. 1994; Farahat et al. 2007; Ali et al. 2016; El-Bialy 2020). Later, mafic to felsic, high-K, Dokhan volcanics (610–580 Ma) and A-type granites (610–560 Ma) were emplaced during the post-collisional extension (Bentor 1985; Hassan and Hashad 1990; Moghazi 2003; Farahat et al. 2007; Ali et al. 2016; Mohamed et al. 2019; El-Bialy 2020).

Local geologic setting

The main volcanic episodes during the Neoproterozoic time in the Eastern Desert of Egypt are represented by metavolcanic and Dokhan volcanic rocks (Akaad and El-Ramly 1960). The metavolcanic rocks characterize the older volcanic episode (~ 770–695 Ma) (e.g., Stern and

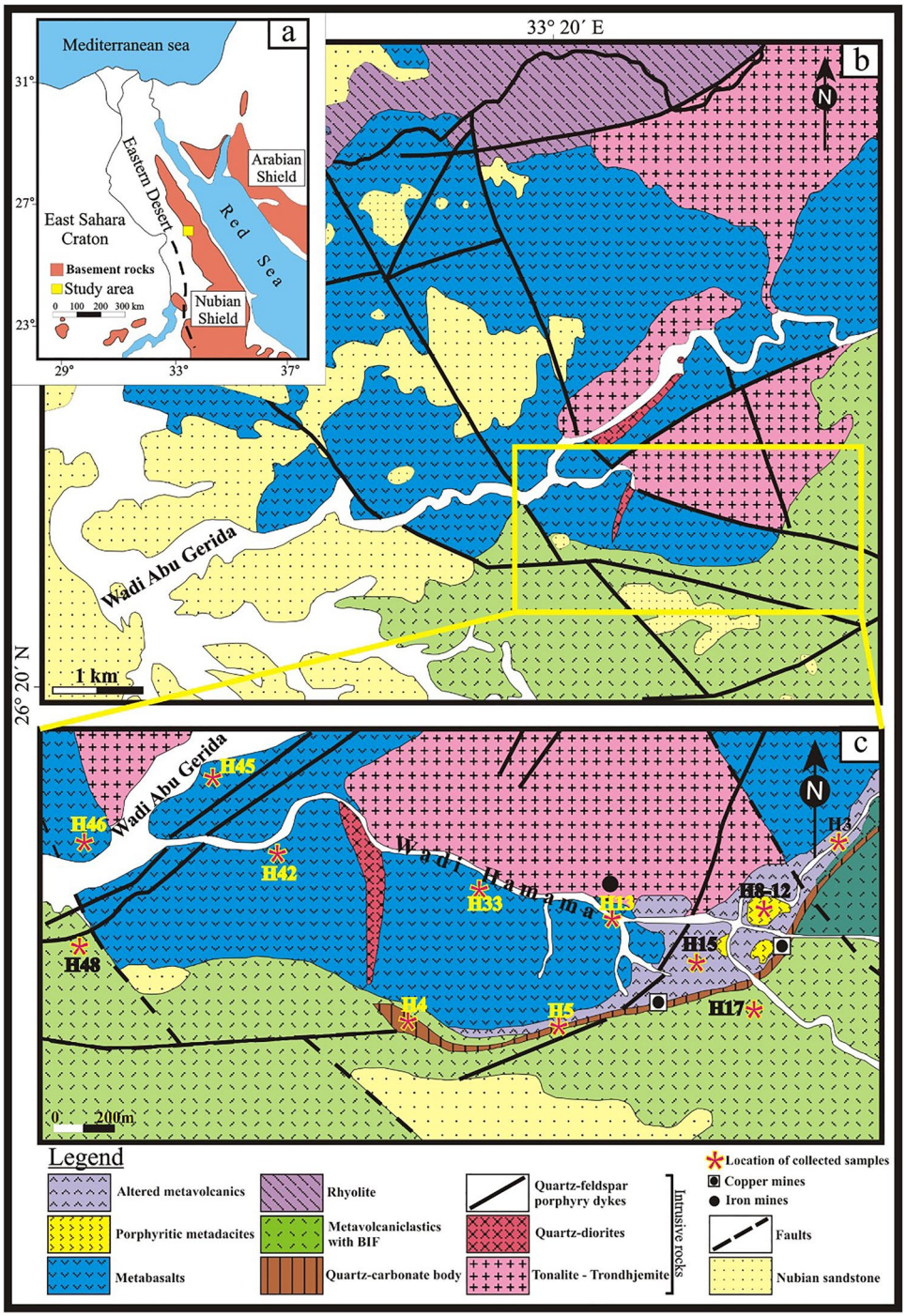

Fig. 1 **a** Location map of the study area. **b** Geologic map of the Wadi Hamama area (Minex Mineral Egypt 1991). **c** Detailed geologic map of the ancient mining area (after Abdel Nabi et al. 1977)

Hedge 1985; Kröner et al. 1992; Ali et al. 2009; Bühler et al. 2014; Abd El-Rahman et al. 2017, 2020; Gamal El Dien et al. 2021). They document the early stages of Neoproterozoic crustal growth in the northern part of the ANS (Ali et al. 2009). Shadli metavolcanic rocks represent the largest metavolcanic occurrences in the Nubian Shield (Shukri and Mansour 1980; Stern et al. 1991). On the other hand, the Dokhan volcanic rocks are unmetamorphosed and represent the younger volcanic episode (614–550 Ma) (Akaad and El-Ramly 1960; El-Gaby et al. 1991; Azer and Farahat 2011).

The Hamama area lies in the CED of Egypt, particularly southwest Safaga (Fig. 1a). This area consists of metavolcanics intruded by syntectonic granites as well as felsic dikes and overlain by Nubian sandstones (Fig. 1b). The metavolcanics, the oldest rock unit in the area, are considered as a member of the Neoproterozoic Shadli metavolcanics. The U–Pb zircon dates from ca. 695 Ma for these rocks,

corresponding to a Cryogenian volcanic episode (Abd El-Rahman et al. 2020). This age is consistent with that given by Gamal El Dien et al. (2021) for Shadli bimodal metavolcanics (~ 700 Ma). These rocks are represented by a series of weakly metamorphosed mafic and felsic varieties. They comprise mainly metabasalts and less common metadacites, metarhyolites, and their tuffs. The NE–SW-trending quartz-feldspar porphyry dikes intrude metabasalts (Figs. 1c, 2a). The metavolcanics host a N–S-trending quartz-specularite vein (Fig. 2b). Sporadic patches of Nubian sandstones non-conformably overlie the metabasalts (Fig. 2c). Metabasalts, the dominant rock type, are mainly massive and sometimes show evidence of epidotization and/or chloritization in the footwall alteration zone. Spilitization is also recorded, especially near the contact with the tonalite–trondhjemite mass. Metadacites and metarhyolites occur as small masses in the southern and northern parts of the area. The altered metavolcanics (Fig. 1c) represent the footwall alteration zone (Abdel Nabi et al. 1977). Porphyritic metadacites occur within the footwall alteration zone that extends along the boundary between the metabasaltic and metavolcaniclastic rocks (Fig. 1c). They were subjected to intense hydrothermal alterations, mainly along the contact with the quartz-carbonate horizon. The intensively altered dacite contains

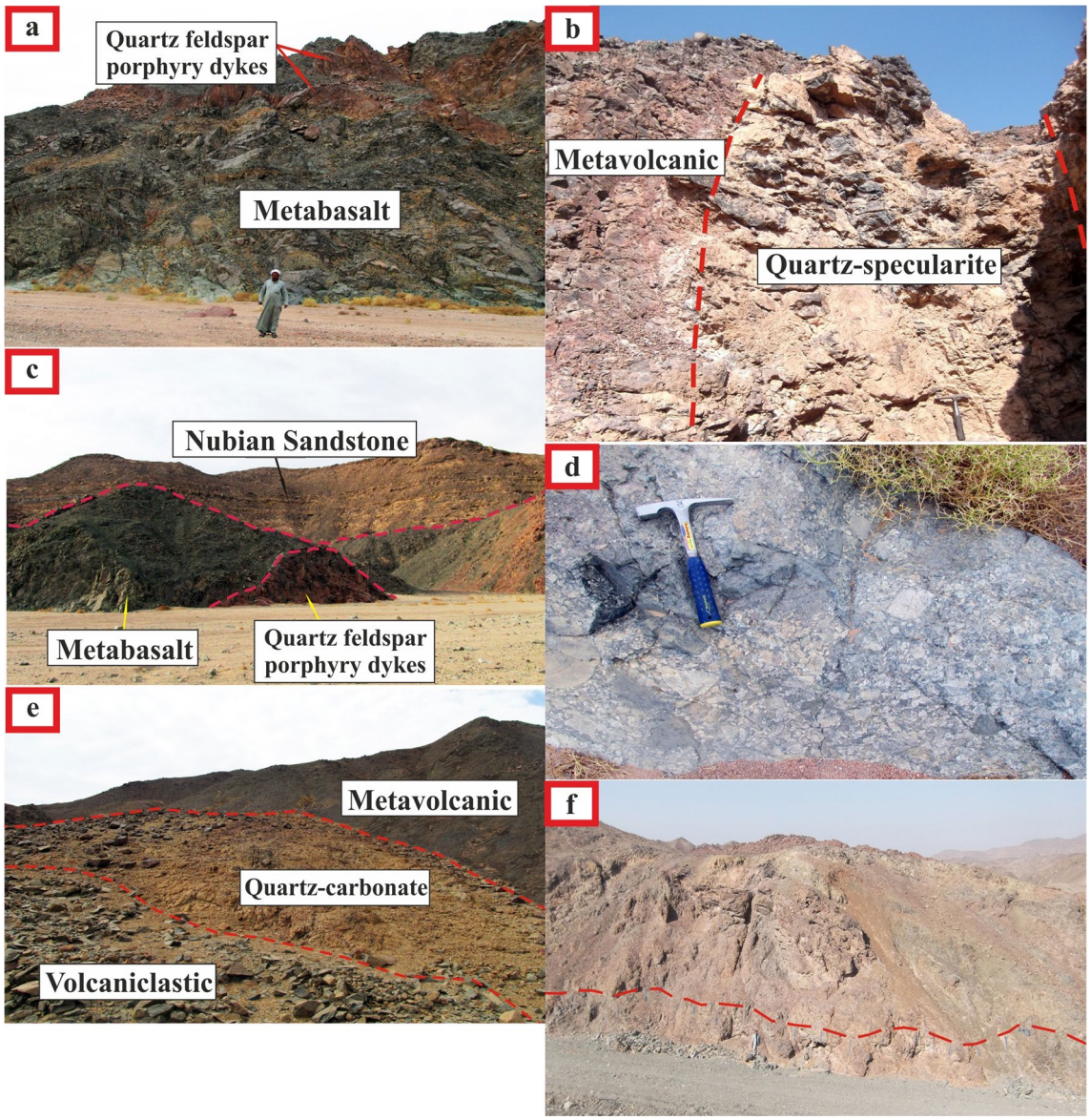

Fig. 2 Field photographs showing **a** metabasalt intruded by quartz-feldspar porphyry dikes, **b** a quartz-specularite vein hosted in metavolcanic rocks, **c** metabasalt non-conformably overlain by Nubian sandstone, **d** a close-up view of volcaniclastic rocks enclosing angular to sub-angular rock fragments, **e** quartz-carbonate exhalites at the contact between metavolcanic and metavolcaniclastic rocks, and **f** quartz-carbonate exhalites with a siliceous zone at the footwall of the Wadi Hamama sequence

fine oxidized pyrite crystals. A rhyolitic dome, up to 100 m thick, has been spatially detected above the VMS zone by teamwork at the company Aton (2012).

Metavolcaniclastic rocks (Fig. 1b, c) crop out in the southern part of the mapped area and form a continuous, E–W-trending, elongate belt. They comprise banded metatuffs, lapilli metatuffs, volcanogenic metagreywackes, and metaconglomerates. These rocks are non-conformably overlain by dispersed patches of Nubian sandstone. Their contact with metavolcanics is gradational, being marked in some parts by the occurrence of quartz-carbonate exhalite. The metavolcaniclastic rocks consist of angular to subangular fragments (up to 15 cm in length) with felsic and mafic compositions (Fig. 2d). Some zones of the banded metatuffs and the volcanogenic greywacke contain primary magnetite- and hematite-rich bands. The quartz-carbonate exhalative horizon that hosts the sulfide deposits extends NE–SW along the contact between the metavolcanic and metavolcaniclastic facies (Fig. 2e). This horizon has a length of ~ 3 km and a varying thickness and shows a siliceous zone in the footwall (Fig. 2f). Volcanogenic sulfide gossan is associated with the exhalites (Minex Mineral Egypt 1991; Hassan 2005; Aton 2012). Quartz-carbonate exhalite in trenches and pits is stained by secondary copper minerals such as malachite (Fig. 3a). The footwall rocks (mainly metaandesites) were strongly altered in the stringer zone to sericite-quartz-pyrite. This stringer zone has abundant quartz-sulfide veins and veinlets that are up to a few hundred meters thick (Aton 2012). Andesitic rocks are generally scarce, like those from bimodal volcanism of a back-arc basin (Abdel-Karim et al. 2019 and references therein). Moreover, they were recorded in the volcanic cycles of the Shadli bimodal metavolcanics (Stern et al. 1991). A few ancient copper mines from Ptolemaic times are located within both the quartz-carbonate exhalative horizon and the alteration zone (Abd El-Rahman et al. 2013; Fig. 1c). Also, a few historical iron mines are located within the quartz-specularite veins that are hosted in the tonalite–trondhjemite mass (Fig. 1c).

Syntectonic granites intrude the metavolcanics and are dissected by quartz-feldspar porphyry dikes (Fig. 3b). They are characterized by exfoliation and boulder weathering. These granites consist of quartz-diorite and tonalite-trondhjemite (Fig. 1c).

Felsic dikes are commonly quartz-feldspar porphyry and occur as swarms trending mainly NE–SW (Fig. 2a). They intrude all rock units and show great extensions up to tens of kilometers long and 10 m wide. Their contact with

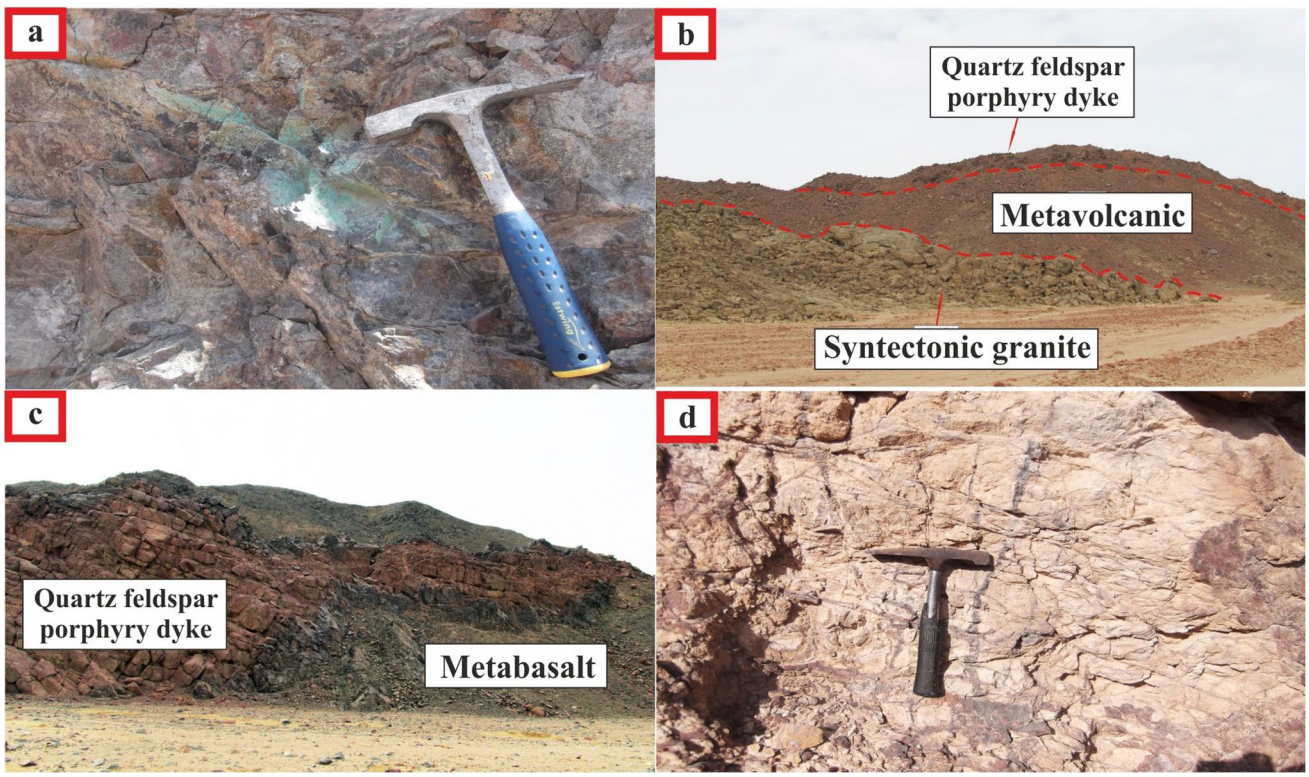

Fig. 3 Field photographs showing **a** malachite staining on quartz-carbonate exhalites, **b** syntectonic granite intruding metavolcanic rocks; both of which are intruded by a quartz-feldspar porphyry dike, **c** a chilled margin at the contact between a quartz-feldspar porphyry dike and metabasalt, and **d** a network of hematite veinlets in the footwall of quartz-carbonate exhalites

metabasalt is characterized by chilled margins due to localized thermal effects (Fig. 3c).

Mode of occurrence of sulfide deposits

The Hamama prospect contains primary hypogene sulfide mineralization covered by an oxidized zone of gold-bearing gossan (Aton 2017). The primary sulfide zone contains up to 3.7 wt% Zn, 0.23 wt% Cu, 2.61 g/t gold, and 150 g/t silver (Aton 2017). The high-grade primary massive sulfide mineralization is divided into three zones: (1) the western VMS zone (the main zone), (2) the central VMS zone, and (3) the eastern VMS zone (Fig. 4a; Aton 2012). The sulfide mineralization occurs as disseminated and as semi-massive to massive deposits. Disseminated sulfide mineralization is easily seen by the naked eye and is hosted mainly by metabasalts and metadacites (Fig. 4b, c). Sulfide grains are mostly composed of pyrite with rare chalcopyrite (Table 1). The semi-massive to massive sulfide mineralization is observed

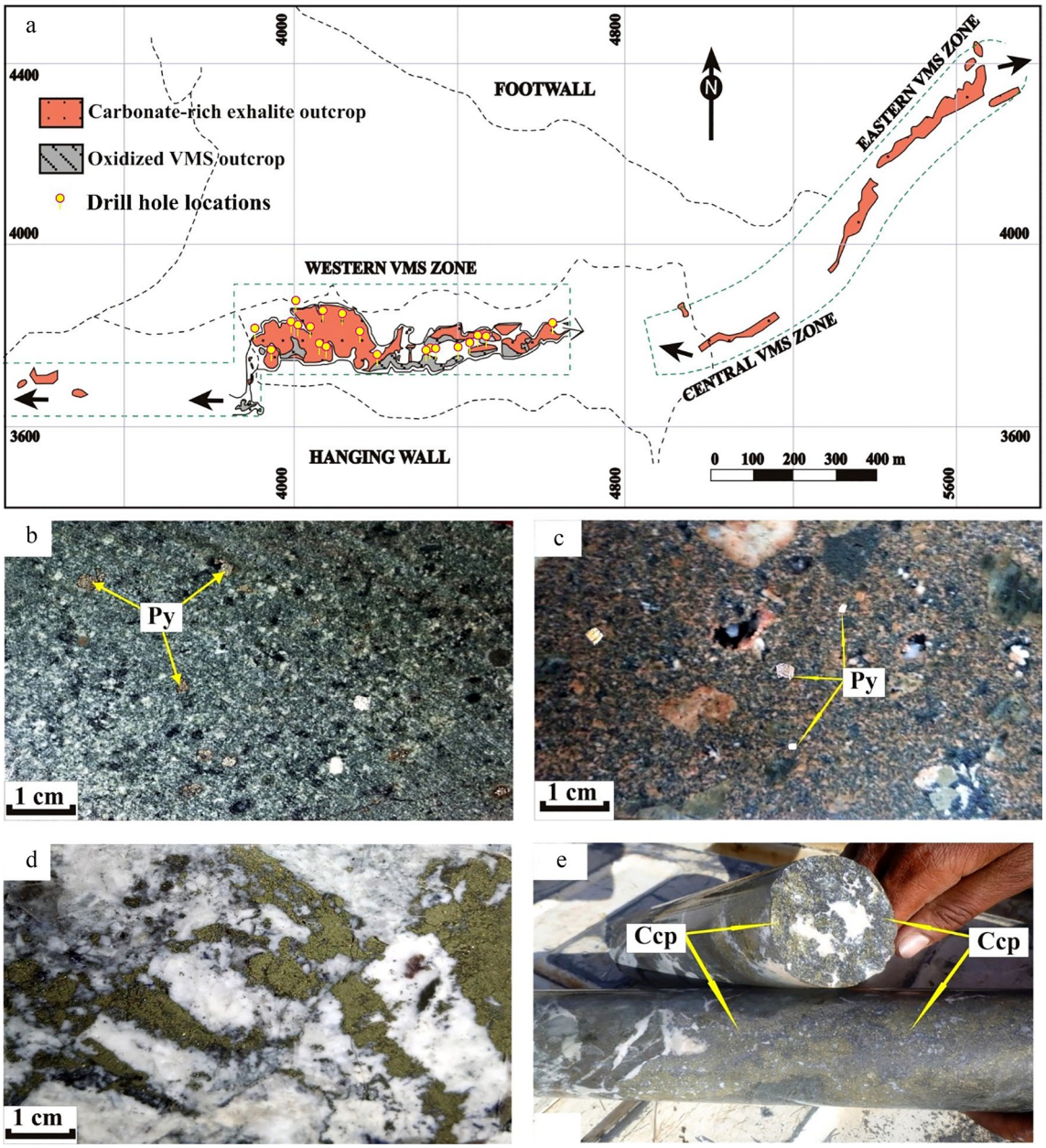

Fig. 4 **a** Sketch map showing the three VMS zones (after Aton 2012). Polished slabs show disseminated pyrite crystals hosted in **b** metabasalt, and **c** metadacite. **d** Polished slab showing semi-massive pyrite-rich veins alternating with carbonates. **e** Chalcopyrite-sphalerite massive sulfide core sample obtained at 160 m depth (after Aton 2012)

Table 1 Types and distribution of Hamama sulfide minerals

Sample number	Petrographic nomenclature	Ore type	Pyrite	Chalcopyrite	Galena	Sphalerite	Polybasite
H.33	Metabasalt	Disseminated	++++	+	–	–	–
H.12	Metadacite		++++	–	–	–	–
H.4	Quartz-carbonate	Semi-massive	++++	–	+++	++	+

++++ Dominant, +++ common, ++ fairly common, + rare, – absent

in the underground levels of Hamama VMS mine and is hosted in and below the quartz-carbonate exhalite horizon. This horizon may have acted as a cap rock, preserving the Zn-rich VMS system and preventing the dissipation of metal-rich hydrothermal fluids (Abd El-Rahman et al. 2015). In trenches and pits, it is characterized by malachite stains (Fig. 3a). In some places on the surface, this horizon is strongly weathered to iron-rich gossan that includes considerable contents of zinc, copper, gold, and silver, while in other places it is weathered to an ankerite-rich rock that contains minor to moderately abundant iron oxides with lesser contents of base and precious metals (Aton 2012). The copper minerals malachite and chrysocolla were observed in very small zones of quartz veining (Aton 2017). Gold and silver are highly abundant in the uppermost part of the quartz-carbonate horizon, likely due to supergene processes (Aton 2017). They are hosted by a quartz network stained with limonite/hematite. Well-developed colored liesegang rings characterize some parts in the siliceous zone of the quartz-carbonate horizon. The growth of these rings is structurally controlled by a conjugate fracture system. Also, a network of hematite veinlets (Fig. 3d) is present in the footwall of the quartz-carbonate horizon. The semi-massive sulfide mineralization is found as small veinlets that fill fractures and alternate with quartz-carbonate rock (Fig. 4d). It consists mainly of pyrite, galena, sphalerite, and polybasite in decreasing order of abundance (Table 1). The exhalite core samples are rich in precious metals (up to 1.36 g/t gold and 50.63 g/t silver: Aton 2012) (Table 4). The massive Zn-rich type from deeper levels of the mine (> 150 m from the surface; Aton 2012) consists mainly of sphalerite and minor chalcopyrite (Fig. 4e). It seems that the base metal changes from Pb to Zn with increasing depth in the prospect.

Sampling and analytical methods

The locations of the samples collected from the Hamama area are presented in Fig. 1c. The sulfide samples were collected from metavolcanics (e.g., metabasalts and metadacites) and from the quartz-carbonate exhalative horizon. Fresh semi-massive sulfide core samples were obtained from holes drilled by Aton.

About 12 polished slabs of sulfide-rich samples were prepared for ore microscopy studies. Electron probe microanalyses (EPMA) were performed on two sulfide-rich samples (H.4 and H.5) (Table 2) using a JEOL Super Probe JXA 8900R electron microanalyzer at Nevada University, Las Vegas, USA. The probe was equipped with a lanthanum boride cathode and operated at 20 kV and 38 nA with beam diameter of 3 µm. The standards were natural sulfides, silver, and gold. EPMA data were corrected by using a ZAF program (Bence and Albee 1968).

The trace elements and REEs of the Cpx in basalt were analyzed in situ by laser ablation (193 nm ArF excimer MicroLas GeoLas Q-plus)–inductively coupled plasma mass spectrometry (Agilent 7500S) (LA–ICP–MS) at Kanazawa University, Japan (Table 3). All analyses were carried out at 6 Hz with an energy density of 8 J/cm^2 per pulse and were performed by ablating 60-µm-diameter spots. ^{29}Si was used as an internal standard based on the SiO_2 concentration obtained by the electron microprobe, and NIST 612 glass was used as an external standard, assuming the composition given by Pearce et al. (1997). A secondary standard (e.g., NIST 614 glass) was analyzed for quality control in every analysis. The reproducibility or precision of analysis was better than 8% for the elements except for Sc and V, for which it was better than 20%. More details about the analytical procedures, accuracy, and standards have been described by Morishita et al. (2005).

Petrography and mineral chemistry

Metavolcanics

Metavolcanics are essentially represented by metabasalt, metadacite, and metarhyolite, together with their pyroclastics. For detailed petrographic features of metavolcanics and the chemistry of their mineral constituents, we refer the reader to Abdel-Karim et al. (2019). The Hamama metadacite in contact with quartz-carbonate exhalite is intensively carbonatized. It is invaded by numerous calcite veinlets and pseudomorphic calcite crystals. It contains fine disseminated oxidized pyrite crystals. The metabasalt surrounding quartz-carbonate exhalite is highly chloritized. The quartz-carbonate exhalite consists mainly of carbonate (calcite and

Table 2 Major and trace elements of Hamama ore minerals hosted in quartz-carbonate rocks

Sample no.	Mineral name	Texture	S	Fe	Cu	Zn	As	Pb	Ag	Au	Sb	Tl	Hg	Cd	Te	Total	Au/As
			(173)	(301)	(402)	(1086)			(540)	(863)							
H.4	Py	Framboidal pyrite	51.94	46.43	0.05	0.06	0.23	–	bdl	0.05	bdl	bdl	bdl	–	–	98.76	0.22
	Py		52.31	45.94	bdl	bdl	0.25	–	0.05	0.06	0.05	bdl	bdl	–	–	98.66	0.24
	Py		51.7	45.09	0.05	bdl	0.33	–	0.1	0.06	bdl	0.05	bdl	–	–	97.38	0.18
	Py		51.62	45.19	0.12	bdl	0.37	–	0.44	0.07	0.07	0.14	0.08	–	–	98.1	0.19
	Py		51.9	45.25	0.07	bdl	0.45	–	0.52	0.08	0.05	0.18	bdl	–	–	98.5	0.18
	Py		50.94	45.05	0.05	bdl	2.14	–	0.55	0.12	bdl	bdl	0.11	–	–	98.96	0.05
	Py	Inclusion	52.34	45.96	bdl	bdl	bdl	–	bdl	bdl	bdl	bdl	0.08	–	–	98.38	–
H.5	Py	Non-framboidal pyrite	52.77	46.28	bdl	bdl	bdl	–	bdl	bdl	bdl	–	–	–	–	99.05	–
	Py		52.65	46.04	bdl	0.07	bdl	–	bdl	bdl	bdl	–	–	–	–	98.76	–
	Py		52.32	45.39	bdl	0.05	bdl	–	bdl	0.06	bdl	0.22	-	–	–	98.07	–
	Py		52.42	45.97	bdl	bdl	bdl	–	bdl	bdl	bdl	–	–	–	–	98.39	–
	Py		52.01	45.9	bdl	0.06	bdl	–	bdl	0.05	bdl	–	–	–	–	98.02	–
	Py		52.38	45.58	bdl	bdl	bdl	–	bdl	0.05	bdl	0.11	–	–	–	98.12	–
	Py		52.65	46.68	bdl	bdl	bdl	–	bdl	bdl	bdl	0.08	–	–	–	99.41	–
	Py		52.45	46.12	bdl	0.1	bdl	–	bdl	bdl	bdl	0.05	–	–	–	98.72	–
	Py		52.8	45.68	bdl	bdl	bdl	–	bdl	0.05	bdl	–	–	–	–	98.53	–
	Py		52.19	46.08	bdl	bdl	bdl	–	bdl	bdl	bdl	0.05	–	–	–	98.32	–
H.4	Sph		33.26	0.53	–	66.28	–	–	bdl	–	–	–	0.09	0.31	–	100.47	–
	Sph		33.31	0.65	–	66.2	–	–	bdl	–	–	–	0.06	0.35	–	100.57	–
	Sph		33.11	0.51	–	66.01	–	–	bdl	–	–	–	0.17	0.32	–	100.12	–
	Sph		32.78	0.48	–	66.97	–	–	bdl	–	–	–	0.09	0.33	–	100.65	–
	Sph		33.43	0.44	–	67.14	–	–	bdl	–	–	–	0.08	0.32	–	101.41	–
	Sph		33.24	0.54	–	67.25	–	–	0.06	–	–	–	0.11	0.35	–	101.55	–
H.5	Sph		33.2	0.47	–	67.74	–	–	bdl	–	–	–	0.08	0.31	–	101.8	–
	Sph		33.08	0.53	–	67.15	–	–	bdl	–	–	–	0.24	0.33	–	101.33	–
	Sph		32.99	0.44	–	66.48	–	–	bdl	–	–	–	0.13	0.32	–	100.36	–
	Sph		33.26	0.5	–	67.09	–	–	bdl	–	–	–	0.23	0.34	–	101.42	–
	Sph		32.76	0.49	–	67.21	–	–	bdl	–	–	–	0.16	0.36	–	100.98	–
	Sph		32.98	0.56	–	67.07	–	–	bdl	–	–	–	0.16	0.29	–	101.06	–
H.4	Gn		13.49	bdl	bdl	bdl	bdl	87.9	bdl	0.12	bdl	0.06	–	–	bdl	101.57	–
	Gn		13.11	bdl	0.16	bdl	bdl	86.26	bdl	bdl	bdl	bdl	–	–	bdl	99.53	–
	Gn		13.21	bdl	bdl	0.05	bdl	86.84	bdl	0.06	bdl	bdl	–	–	bdl	100.16	–

Table 2 (continued)

Sample no.	Mineral name	Texture	S	Fe	Cu	Zn	As	Pb	Ag	Au	Sb	Tl	Hg	Cd	Te	Total	Au/As
H.5	Gn		13.01	0.17	bdl	0.07	bdl	85.75	bdl	bdl	bdl	bdl	–	–	bdl	99	–
	Gn		12.9	bdl	bdl	bdl	bdl	86.04	bdl	bdl	bdl	0.2	–	–	bdl	99.14	–
	Gn		13.03	0.05	0.05	bdl	bdl	86.39	bdl	bdl	bdl	bdl	–	–	bdl	99.52	–
	Gn		13.03	bdl	bdl	bdl	bdl	86.03	bdl	0.11	bdl	bdl	–	–	bdl	99.17	–
H.4	Pol		15.59	bdl	7.87	0.05	2.27	bdl	67.32	bdl	6.81	0.05	–	–	bdl	99.96	–
	Pol		15.95	bdl	8.74	bdl	3.13	bdl	65.17	bdl	5.08	bdl	–	–	bdl	98.07	–
H.5	Pol		13.89	0.09	6.63	bdl	1.67	bdl	71.91	bdl	4.48	bdl	–	–	0.37	99.04	–
	Pol		16.09	bdl	6.2	bdl	1.86	bdl	65.84	bdl	8.42	bdl	–	–	0.48	98.89	–
	Pol		15.4	bdl	7.48	bdl	2.05	bdl	68.52	bdl	4.87	bdl	–	–	0.43	98.75	–

Values in parentheses are the detection limits in ppm

bdl below the detection limit, *Py* pyrite, *Sph* sphalerite, *Gn* galena, *Pol* polybasite

Table 3 Trace element compositions of the studied clinopyroxene from Hamama metabasalt

Element	H.33			dl
	Spot 1	Spot 2	Spot 3	
Li	5.52	7.12	35.36	0.27
B	16.18	22.14	20.10	0.98
Sc	172.84	201.36	141.77	0.059
Ti	1615	1243	1787	0.311
V	263.88	177.81	364.14	0.045
Cr	67.14	14.75	267.25	1.378
Co	49.97	49.37	58.43	0.019
Ni	36.21	20.10	65.05	0.485
As	0.55	0.38	0.41	0.388
Rb	0.14	bdl	0.26	0.035
Sr	9.63	7.70	8.13	0.0061
Y	37.31	50.37	21.84	0.0058
Zr	20.10	20.56	13.03	0.012
Nb	0.05	0.02	0.02	0.0083
Cs	bdl	bdl	0.05	0.018
Ba	1.40	bdl	0.46	0.053
Hf	1.01	0.88	0.62	0.028
Ta	bdl	bdl	bdl	0.011
Pb	0.15	0.12	bdl	0.087
Th	0.02	bdl	bdl	0.0109
U	bdl	bdl	bdl	0.0122
La	1.47	1.82	0.69	0.004
Ce	7.81	10.31	3.98	0.003
Pr	1.59	2.10	0.83	0.0027
Nd	10.29	13.36	5.47	0.0235
Sm	4.22	5.56	2.36	0.0239
Eu	0.62	0.63	0.47	0.0078
Gd	5.87	7.65	3.19	0.0313
Tb	1.03	1.40	0.61	0.0063
Dy	7.43	9.99	4.31	0.0175
Ho	1.53	2.04	0.84	0.0075
Er	4.41	5.92	2.63	0.0118
Tm	0.63	0.86	0.37	0.006
Yb	4.29	5.89	2.54	0.023
Lu	0.60	0.83	0.37	0.0053

dl detection limit, *bdl* below the detection limit

magnesite) and quartz, with minor kaolinite, sericite, chlorite, and Fe oxides/hydroxides. It has a significant amount of sulfides. Pyrite crystals are widely distributed along bands of the colloform carbonates. Highly altered felsic volcanics (silicic-calcic alterations) with disseminations of oxidized pyrite cubes are recorded as being found within the exhalite. The lower part of the exhalite is more enriched in quartz (silicified) and has higher concentrations of sulfides. The metaandesite below the exhalite horizon is highly altered to sericite-quartz-pyrite.

Sulfides and clinopyroxene

Pyrite hosted in metavolcanic and quartz-carbonate rocks forms anhedral to euhedral crystals of various sizes (up to 4 mm in diameter) and random orientations (Fig. 5a), reflecting multiple growth stages. It is a major constituent of semi-massive sulfide mineralization and occurs as fine aggregates that fill fractures in carbonates (Fig. 5b) and as large patches. Sometimes, pyrite crystals occur as small inclusions within galena and sphalerite (Fig. 5c) and show irregular contact with sphalerite. Framboidal (raspberry-like) pyrite is common and occurs as spherical or sub-spherical equidimensional microcrystals (Fig. 5d). It is partially recrystallized to euhedral crystals (Fig. 5d) and sometimes found along sphalerite grain boundaries. Galena hosted in quartz-carbonate rocks occurs mainly as isolated anhedral to subhedral crystals, with a few euhedral ones. Sometimes, it shows irregular contact with pyrite-sphalerite (Fig. 5e). It is occasionally found as a fracture filling within a carbonate matrix (Fig. 5f) and as small anhedral grains enclosed in sphalerite veinlets. Sphalerite is abundant in the quartz-carbonate core samples (Fig. 4e) and occurs mostly as anhedral patches (Fig. 5c). It also occurs as small cross-cutting veinlets that fill fractures (Fig. 5g) and hosts small galena crystals. It has irregular contacts with galena and pyrite grains (Fig. 5c, e). Chalcopyrite, which is a brassy yellow color, is observed in metabasalts and in quartz-carbonate core samples (Fig. 4e). It occurs as disseminated anhedral crystals and as fine specks (Fig. 5h) and is associated with pyrite. The textural relationships between sulfides in the quartz-carbonate horizon indicate two stages of crystallization. In the first stage, pyrite is the earliest sulfide phase and comprises framboidal and recrystallized varieties (Fig. 5d). Sphalerite and galena were formed later than pyrite, with both containing fine pyrite inclusions (Fig. 5c). The mutual relation boundary between sphalerite and galena probably suggests simultaneous crystallization. The second stage is represented by veinlets of pyrite, sphalerite, and galena that cross-cut a mineral assemblage of the first stage (Fig. 5f,

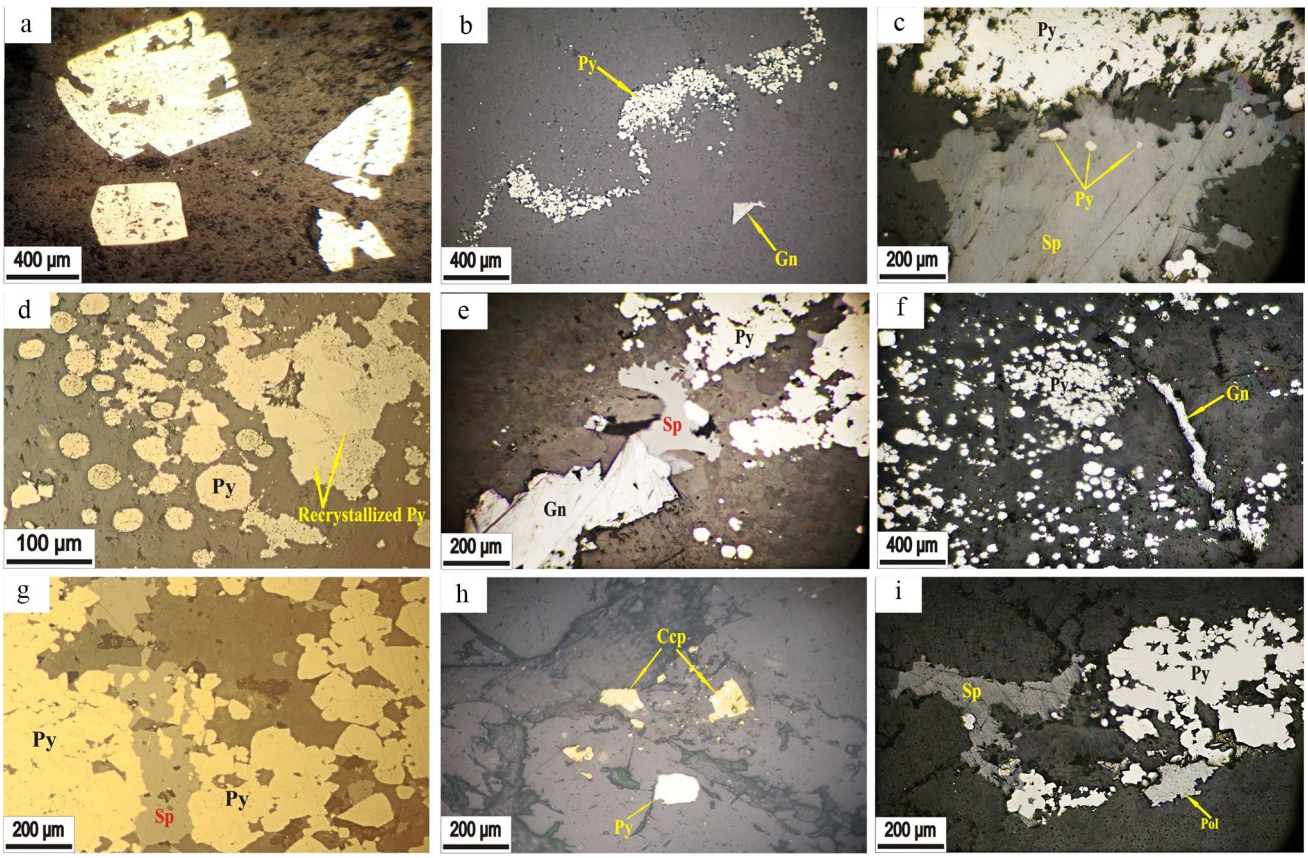

Fig. 5 Reflected light photomicrographs of sulfides hosted in metavolcanics (**a** and **h**) or quartz-carbonates (**b–g** and **i**). **a** Pyrite crystals of different sizes and shapes. **b** Fine disseminated pyrite clusters filling a fracture in carbonates; note the galena triangular section. **c** Irregular contact between pyrite and sphalerite. **d** Numerous spherical framboidal pyrite crystals that are partly recrystallized to euhedral ones. **e** Irregular contact between an anhedral crystal of galena and sphalerite. **f** Framboidal pyrite with galena veinlets. **g** A sphalerite veinlet cutting through pyrite. **h** Fine specks of pyrite and chalcopyrite. **i** Anhedral crystals of polybasite and sphalerite exhibit irregular contacts with pyrite. *Py* pyrite, *Ccp* chalcopyrite, *Sp* sphalerite, *Gn* galena, *Pol* polybasite

g). Silver-bearing sulfosalts are represented by polybasite, which is grayish white in color and occurs as small anhedral crystals. Polybasite sometimes shows irregular contacts with pyrite or galena (Fig. 5i) and probably arose through late hypogenic formation.

The analyzed sulfide minerals of semi-massive deposits hosted in quartz-carbonates include pyrite, sphalerite, galena, and polybasite as well as the associated precious metals (silver and gold) (Table 2). Pyrite contains mainly Fe (45.05–46.68 wt%) and S (50.94–52.8 wt%) (Table 2). It has low Cu (below the detection limit (bdl)–0.12 wt%), Zn (bdl–0.10 wt%), As (bdl–2.14 wt%), Au (bdl–0.12 wt%), and Ag (bdl–0.55 wt%) contents. Heavy metals are undetected except in some samples that show low concentrations (e.g., Hg = 0.08–0.11 wt%; Tl = 0.05–0.22 wt%). Framboidal pyrite is distinguished by its lower S (50.94–52.31 wt%) and higher As (0.23–2.14 wt%), Au (0.05–0.12 wt%), and Ag (bdl–0.55 wt%) compared with non-framboidal pyrite (Table 2). Sphalerite contains narrow ranges of Zn (66.01–67.74 wt%) and S (32.76–33.43 wt%) concentrations (Table 2). The minor and trace element values are controlled by the similarity in size to the tetrahedrally coordinated Zn^{2+}. The Fe^{2+} (0.44–0.65 wt%) and Cd^{2+} (0.29–0.36 wt%) concentrations are low, indicating that they only rarely replace Zn. Mercury (0.06–0.24 wt%) and silver (bdl–0.06 wt%) are found in detectable trace amounts (Table 2). Galena is composed mainly of Pb (85.75–87.9 wt%) and S (12.9–13.49 wt%) (Table 2). Some analyses found high Au contents (0.06–0.12 wt%), like those in galena in the Darhib massive mineralization (up to 0.11%; Abdel-Karim et al. 2022). A few samples have up to 0.2 wt% thallium (Table 2). Polybasite is a silver-bearing sulfosalt and an endmember of the pearceite-polybasite series. It is composed of Ag (65.17–71.91 wt%), S (13.89–16.09 wt%), Cu (6.20–8.74 wt%), Sb (4.48–8.42 wt%), and As (1.67–3.13 wt%) (Table 2).

Cpx trace element compositions of Hamama metabasalt are listed in Table 3. The total REE concentrations range from 28.66 to 68.36 ppm (Table 3). Chondrite-normalized REE values show flat HREE patterns [$(Tb/Lu)_N = 1.12–1.17$] with depletion in LREEs [$(La/Lu)_N = 0.20–0.26$]. The Cpx REE patterns are somewhat like those of Cpx from Kilauea tholeiites (Fig. 6a; Norman et al. 2005). The HREE patterns of Kilauea Cpx are slightly steeper compared to the studied Cpx (Fig. 6a). Strong negative Eu anomalies are observed in Hamama Cpx (Fig. 6a). Primitive mantle-normalized trace element patterns resemble those of Cpx in Kilauea tholeiites except for Pb and Ti (Fig. 6b). Hamama Cpx is characterized by high depletions of High field strength elements (HFSE) (Nb, Zr, and Ti), Sr, and Pb (Fig. 6b).

Discussion

Petrogenesis and tectonic implications of sulfide-bearing rocks

The flat HREE patterns of Cpx in Hamama metabasalts (Fig. 6a) possibly suggest generation from a garnet-free mantle source. This is in harmony with the HREE patterns of the host basalts (Fig. 6c), suggesting formation at a relatively shallow depth, i.e., < ~ 85 km (Abdel-Karim et al. 2019). The LREE depletion [$(La/Lu)_N = 0.20–0.26$], along with the low HFSE contents, likely indicates the derivation of the host basalt from a depleted mantle source. The strong negative Eu anomaly of the investigated Cpx (Fig. 6a) is probably attributable to the tendency of Eu to be incorporated into the Ca site of plagioclase that was simultaneously crystallized with Cpx.

The Cpx REE patterns of Hamama metabasalts resemble those of Kilauea tholeiites (Fig. 6a), possibly suggesting tholeiitic character of their host basalts. The depletion in

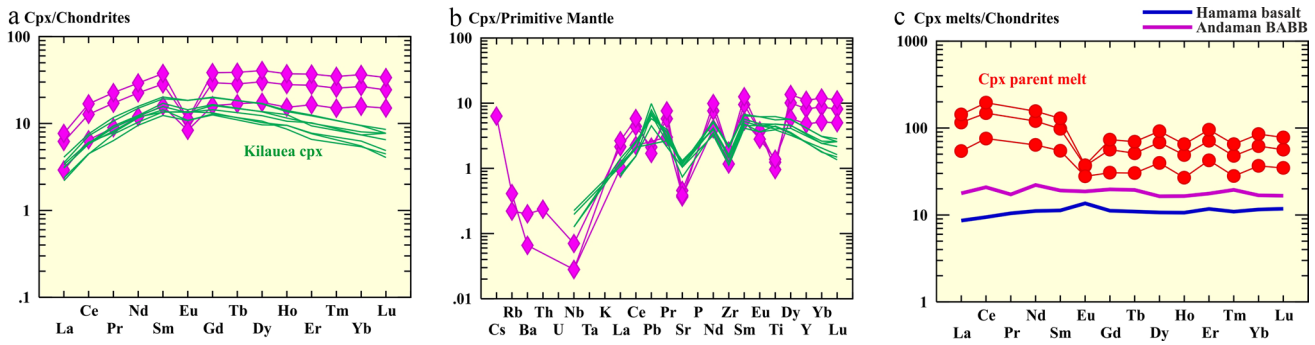

Fig. 6 Cpx trace element compositions in metabasalt. **a** Chondrite-normalized REE patterns. **b** Primitive mantle-normalized trace elements patterns. Kilauea Cpx is from Norman et al. (2005). **c** Chondrite-normalized REE patterns for calculated melts in equilibrium with Hamama Cpx. The Cpx/melt partition coefficients are from Hart and Dunn (1993) and Stosch (1982). Average compositions of Andaman back-arc basin basalt (BABB) from the Indian Ocean (Saha et al. 2019) and Hamama basalt from the Eastern Desert (Abdel-Karim et al. 2019) are shown for comparison. Normalizing values are from McDonough and Sun (1995)

HFSEs (Nb, Zr, and Ti) (Fig. 6b) of Cpx reflects the arc-like signature of the host basalts (Khedr et al. 2020). High boron concentrations (B = 16.18–22.14 ppm) suggest a contribution from subducted sediments in an arc setting (Leeman 1996). The observed negative anomalies for Nb, Sr, and Zr (Fig. 6b) resemble Kilauea Cpx of rift-related origin (Norman et al. 2005).

The compositions of melts in equilibrium with Cpx in Hamama basalts (Fig. 6c) were calculated using the Cpx/melt partition coefficients (Hart and Dunn 1993; Johnson 1998). The Cpx parent melt compositions exhibit nearly flat chondrite-normalized REE patterns like Andaman back-arc basin basalt (BABB) from the Indian Ocean, which was crystallized from tholeiitic basaltic melts (Saha et al. 2019) (Fig. 6c). This probably indicates that the Hamama Cpx was crystallized from tholeiitic melts in a back-arc basin setting (e.g., Khedr et al. 2023).

The bulk-rock geochemistry of Hamama metabasalts, alongside the major element data for pyroxene, indicates an affinity for the tholeiitic suite and suggests crystallization from a depleted mantle source modified by subduction-related slab fluids/melts (Abdel-Karim et al. 2019; Khedr et al. 2023). This is consistent with Abd El-Rahman et al. (2015), who indicated that Hamama sulfides were mostly hosted by tholeiitic bimodal metavolcanics with geochemical characteristics of the island-arc setting. The parental magmas of Shadli metavolcanics were produced by a depleted mid-ocean ridge basalts (MORB)-like source that had suffered from hydrothermal alteration by fluid circulation in an oceanic environment (Gamal El Dien et al. 2021; Khedr et al. 2023). They proposed a rift-related setting for Shadli metavolcanics. Abdel-Karim et al. (2019), based on geochemical data from Hamama metabasalts, inferred that formation occurred in a back-arc setting. This inference is in harmony with pyroxene REE data (Fig. 6c). The piling up of the generated mafic magma below the arc can lead to partial melting of the crust and the formation of the felsic metavolcanic rocks (Hart et al. 2004). The felsic metavolcanics, especially dacites, act as heat engines that are responsible for the circulation of the hydrothermal fluids which form Hamama VMS deposits (Abd El-Rahman et al. 2015).

The VMS deposits seem to have formed in an extensional tectonic regime, such as at mid-ocean spreading centers, back-arc spreading centers, and intra-continental rifts (Ohmoto 1996). A hydrothermal system of island arcs is generated at shallow depths and usually lower-temperature conditions compared to those at mid-ocean ridges (Hannington et al. 2005). So, the domination of Zn and Ag, which are likely transported to and concentrate in a low-temperature environment, implies the generation of Hamama VMS deposits at a shallow water depth during the rifting of intra-oceanic island arcs (e.g., Abd El-Rahman et al. 2015). Based on the presented data, the studied sulfide-bearing rocks were developed from tholeiitic melts in a back-arc spreading cente—a favored tectonic environment for Hamama VMS deposits.

Classification and role of the supergene enrichment of Hamama VMS

The VMS deposits are classified into mafic, pelitic-mafic, bimodal-mafic, felsic-siliciclastic, and bimodal-felsic according to the host-rock assemblage (Franklin et al. 2005). Mafic rocks dominate the first three groups, whereas felsic rocks are prevalent in the last two groups. The lack of ophiolitic rocks in the Hamama prospect, together with the massive nature of the basaltic flows, argues against an ophiolitic nature of the Hamama mafic rocks (e.g., Abd El-Rahman et al. 2015). So, Hamama VMS deposits can be classified as bimodal-mafic (Franklin et al. 2005) because the host metabasalt is the dominant rock type covering > 50% of the area and is only rarely associated with metadacite and metarhyolite (Abd El-Rahman et al. 2015; Abdel-Karim et al. 2019). They resemble other bimodal-mafic districts that host VMS deposits in Noranda (Santaguida et al. 1998), Abitibi (Hannington et al. 2003), and Flin Flon (Bailes and Galley 1999). These districts, including the Hamama area, contain subordinate volcaniclastic rocks characterized by an immature nature (Abd El-Rahman et al. 2015).

In addition to the present field, petrographic, sulfide mineral chemistry, and Cpx trace element data, we used geochemical data from Aton (2012, 2017) to precisely define the type of VMS mineralization in the Hamama prospect. The published data (Table 4) comprise both diamond drilling samples that are less affected by supergene alteration and surface trench samples that are variably affected by weathering processes. The analyzed fresh samples (Table 4) collected from diamond drilling are plotted in the base-metal field (Fig. 7a; Hannington et al. 1999). Based on metal contents, the VMS deposits include three categories, namely Cu, Zn–Cu, and Zn–Pb–Cu deposits (Large 1992). Accordingly, Hamama VMS deposits are classified as Zn–Cu-type deposits with distinctly low Cu and high Zn contents (Table 4; Fig. 7b, c). They exhibit high Zn/Cu ratios (11–117) and low Cu/(Cu + Zn) ratios (0.008–0.081). Consequently, the Hamama prospect can be further classified as a Zn-rich VMS deposit.

Metals in fluids of the hydrothermal system result mainly from the process of leaching acting on the hydrothermally altered rocks (Ohmoto 1996). So, the metal contents in the VMS deposits are affected by the composition of the host rock (Doe 1994). Fluids in the hydrothermal vent of the mafic-dominant environment show high Cu concentrations (Hannington et al. 2005). Hence, the high Zn/Cu ratios may suggest an ineffective Cu leaching process compared to that of Zn from Hamama basalts, which preserves some

Table 4 Representative chemical analyses of Hamama VMS deposits (after Aton 2012, 2017)

Hole no.	Zone (western VMS)	Depth (m)		Zn (%)	Cu (%)	Pb (%)	Ag (g/t)	Au (g/t)
		From	To					
T-085	Gossan (3–5 m) from trenches	–	–	3.73	–	0.08	0.01	43
		–	–	0.90	–	0.15	0.05	10.5
		–	–	0.80	–	0.04	-	7.3
		–	–	0.53	–	0.13	0.01	22
T-086		–	–	0.76	–	0.26	0.08	48
		–	–	2.89	–	0.19	0.03	51.1
AHA-006	Partly altered oxidized zone	26	28	1.17	0.01	–	0.75	0.24
AHA-008		37	39	2.54	0.12	–	15.20	0.26
AHA-009		21	30	2.49	0.22	–	11.01	0.19
		22	26	3.60	0.23	–	5.50	0.13
AHA-003	Primary sulfide zone	89	100	4.11	0.19	–	30.70	0.29
		91	96	7	0.27	–	49	0.37
AHA-004		108	122	6.54	0.30	–	47.05	0.81
		110	118	10.21	0.34	–	45.85	0.73
AHA-005		127	142	4.92	0.21	–	32.35	0.72
		127	130	11.85	0.41	–	50.63	1.36

For all chemical analyses, we refer the reader to Aton (2012, 2017)

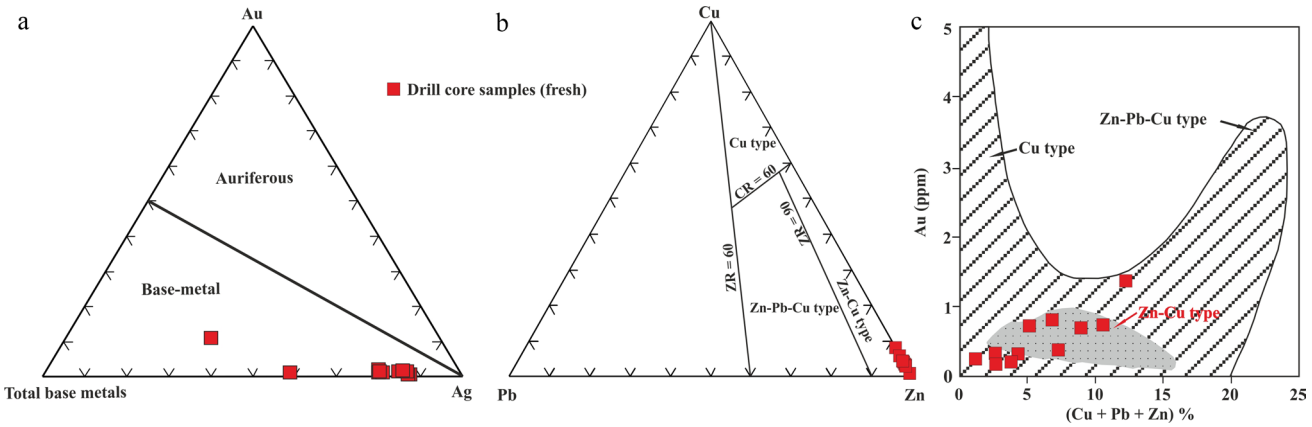

Fig. 7 **a** Au–Ag–(base metals) ternary plot of the Hamama VMS (Hannington et al. 1999), **b** Pb–Cu–Zn ternary discrimination diagram of VMS types, and **c** the variation of the Au content with the base metal contents of Hamama ore. The VMS types are after Large (1992). The data source is after Aton (2012)

disseminated primary chalcopyrite (Abd El-Rahman et al. 2015). Also, the metal contents rely on the temperature conditions of the fluid (Ohmoto et al. 1983). Zinc enrichment indicates a low temperature of Zn-bearing ore formation because Zn is soluble at a lower temperature compared with Cu (Ohmoto et al. 1983). So, the enrichment of Zn relative to Cu in the Hamama prospect suggests that low-temperature hydrothermal fluids played a major role in their formation (Ohmoto et al. 1983; Abd El-Rahman et al. 2015). The Hamama prospect also has significant precious metal (Ag and Au) concentrations (Table 4), which are common in low-temperature vent systems that produce Zn-rich hydrothermal deposits (Herzig and Hannington 1995). The existence of carbonate in the Hamama prospect endorses the low-temperature nature of the hydrothermal system (e.g., Large and Both 1980).

The analyzed sulfide samples from the trench are rich in gold (Au contents of up to 51.1 g/t; Table 4), which is a result of oxidation and leaching from the upper part of the quartz-carbonate horizon (gold-bearing gossan). The gold enrichment indicates the importance of subaerial weathering for gossan formation in the studied VMS. Gold and silver are enriched in the weathered uppermost part of the quartz-carbonate horizon (Aton 2017). Copper is also detected at low concentrations in the gossan zone, where copper oxides (malachite and chrysocolla) are generally restricted

to fracture planes (Aton 2017). The partly oxidized sulfide zone also exhibits high sulfide metal contents—especially that of Zn (up to 3.6 wt%; Table 4) due to the presence of Zn-bearing minerals, which are related to the original distribution of sphalerite prior to the weathering events. Accordingly, Hamama mineralization can be classified as polymetallic VMS deposits (i.e., Zn–Cu–Ag–Au VMS) of bimodal-mafic type.

Role of hydrothermal fluids in the accumulation of Ag- and Au-bearing sulfide deposits

Several VMS districts are characterized by the occurrence of high-level subvolcanic intrusions, which have been proposed to represent a probable heat engine driving the mineralizing hydrothermal systems (Large et al. 1996; Galley 2003; Whalen et al. 2004). The quartz-feldspar porphyry dikes in the Hamama prospect intruded both the footwall alteration zone and the metavolcaniclastic rocks of the hanging wall, so the subvolcanic intrusions that perhaps accounted for the hydrothermal convection could have been the porphyritic dacite, the tonalite-trondhjemite, or the quartz-diorite intrusions (Fig. 1c). Generally, the subvolcanic intrusions, which behave as heat engines, show two main features: (1) an absence of a substantial metamorphic aureole because of the convective heat transfer during crystallization (Cathles et al. 1997) and (2) the presence of fracture-controlled alteration assemblages in the intrusions (Galley 2003). These two traits are shown in both the porphyritic dacite and the tonalite-trondhjemite, but not in the quartz-diorite (Abd El-Rahman et al. 2015). The pyrite–chlorite–quartz veins mainly cut across the porphyritic dacite, whereas the epidote-quartz and hematite veins cut across the tonalite-trondhjemite. The spatial association of the porphyritic dacite and the hydrothermally altered footwall volcanic rocks (Fig. 1c) suggest that the dacite, or its corresponding at deeper magma chamber, likely represents the heat engine which prompted the formation of the Hamama VMS deposits.

The Hamama footwall alteration zone exhibits a mushroom shape (Fig. 1c), reflecting the prevalence of basaltic lava flows over volcaniclastic layers. The alteration zone shows a siliceous core surrounded by a chlorite zone. The chlorite zone characterizes the footwall alteration zone in several VMS deposits (e.g., Riverin and Hodgson 1980), whereas the siliceous core is uncommon in the footwall alteration zones of many VMS deposits (e.g., Gemmell and Fulton 2001; Khedr et al. 2023). A brecciated carbonate zone composed of large carbonate blocks with a restricted lateral extension overlies the footwall alteration. This likely represents talus blocks or debris flows typical of synvolcanic faults associated with the footwall alteration zones of VMS deposits (Franklin et al. 2005).

Quartz-carbonate exhalites define the boundary between the footwall-altered metavolcanics and the overlying volcaniclastic rocks (Fig. 1c) and mark a break in volcanism (Abd El-Rahman et al. 2015). They are recorded in some VMS deposits (DeMatties 1994; Halley and Roberts 1997; Doyle and Allen 2003; Khedr et al. 2023). Their formation is attributed either to the degassing of magmatic CO_2 or to mixing between a small amount of magmatic CO_2-rich fluids and seawater (Callaghan 2001). The low-temperature sulfide assemblages (framboidal pyrite, Fe-poor sphalerite, galena, and polybasite) are hosted in submarine quartz-carbonate exhalites in the Hamama prospect, suggesting deposition at or near the seafloor due to mixing between low-temperature hydrothermal fluids and seawater (Abd El-Rahman et al. 2015). These exhalites resemble those recognized in Mount Julia-Henty gold deposits (Callaghan 2001), the Bisha district (Barrie et al. 2007), the Matagami district (Liaghat and MacLean 1992), and the Brunswick horizon deposits in Bathurst (Peter and Goodfellow 1996).

Sub-seafloor VMS deposits can be formed either by the dispersion of hydrothermal fluids through preexisting open spaces or by the replacement of the invaded rocks (Doyle and Allen 2003; Piercey et al. 2014). The quartz-carbonate exhalites in the Hamama prospect may represent a trap for hydrothermal fluids, which deposited their metalliferous lode in the preexisting spaces or replaced the chemically reactive carbonates. The occurrence of a few exploited pits in the chlorite alteration zone below the exhalites may suggest the trapping of metals in the stockwork chlorite zone and accumulation close to the paleo-seafloor surface (e.g., Inverno et al. 2008).

Cu and Zn metal zonation was documented in several VMS deposits (Hannington et al. 1995; Herzig and Hannington 1995). The secondary Cu enrichment (e.g., malachite) of the exploited trenches in the exhalites (Fig. 3a) and in the chlorite footwall alteration zone possibly implies the occurrence of a local Cu-enriched zone that serves as a feeder zone in the Zn-rich VMS deposits of the Hamama prospect. This feeder zone was produced from higher temperature fluids compared to the remains of the hydrothermal system and is characterized by Cu enrichment compared with Zn (e.g., Huston et al. 1992; Petersen et al. 2000). The secondary Cu mineralization in the Hamama prospect exists in the iron-rich gossan zone, and its enrichment in the exploited trenches and pits resulted from a supergene process. This supergene zone results either from seafloor weathering or from subaerial weathering (Koski 2012). The higher gold concentrations in the trench samples compared to those in the drilled core samples (Table 4) and the presence of primary sulfide minerals in the core samples (Fig. 4e) (Aton 2012) argue for the role of subaerial weathering in the gossan formation in the Hamama prospect.

The studied pyrite is distinguished based on its arsenic content into As-bearing pyrite (0.23−2.14 wt% As; Table 2) and As-free pyrite. As-bearing pyrite has a framboidal texture, whereas As-free pyrite shows a recrystallized texture (Fig. 5d). The framboidal texture is attributed to rapid nucleation caused by mixing hydrothermal fluids with colder seawater at or near the seafloor (Ohmoto 1996; Butler et al. 1999). Arsenic substitution at the expense of S is indicated by the negative correlation between As and S (Fig. 8a) and is explained by the incorporation of As as AsS within the pyrite crystal lattice (Blanchard et al. 2007). Gold-bearing pyrite is commonly associated with arsenic enrichment because gold solubility increases with arsenic enrichment (Simon et al. 1999; Reich et al. 2005; Deditius et al. 2014). As-bearing pyrite is the major gold- and silver-bearing mineral in the Hamama prospect, where the gold and silver concentrations can reach up to 0.12 wt% and 0.55 wt%, respectively (Table 2). The Au and Ag show a positive correlation (Fig. 8b), and both of them increase as the As content of the pyrite increases (Fig. 8c, d). Reich et al. (2005) stated that the maximum possible amount of gold in a pyrite solid solution depends on the As content in

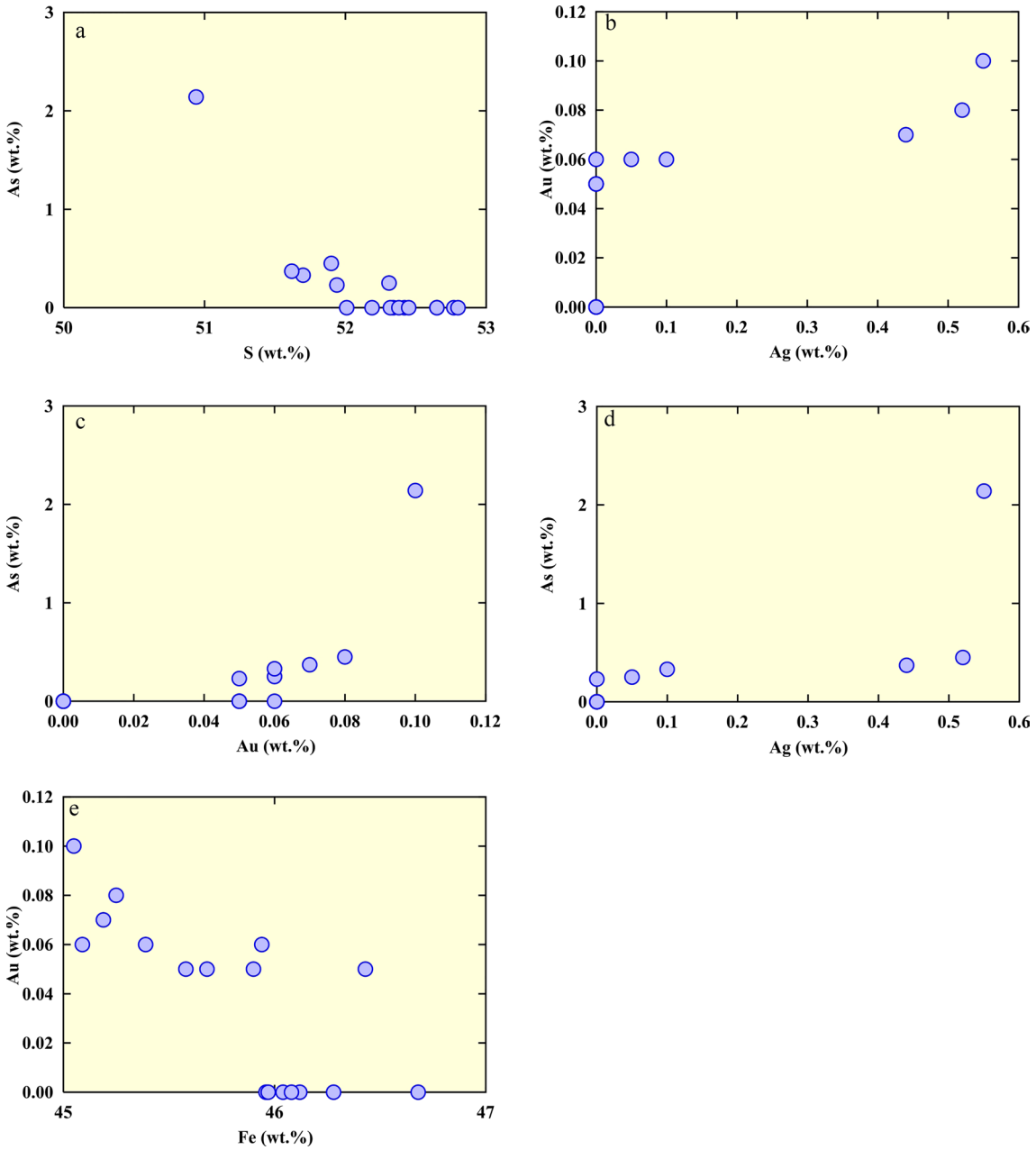

Fig. 8 Pyrite compositions plotted on **a** S–As, **b** Au–Ag, **c** Au–As, **d** Ag–As, and **e** Fe–Au diagrams

the pyrite. This agrees with our results, which indicate that the Au content increases with increasing As content in the As-bearing pyrite relative to the As-free pyrite (Table 2). Consequently, the solubility of Au in As-free pyrite is very low (~2 ± 1 ppm of Au at 500 °C and 1 kbar; Tauson 1999). Arsenic, an important fluid (i.e., mobile) element, plays a very important role in the mobility and accumulation of gold and silver in pyrite, as can be deduced from the high concentrations of Ag and Au in As-bearing pyrite (Table 2; Fig. 8c, d). The Au/As molar ratios (0.05–0.24) in As-bearing pyrite (Table 2) reflect the presence of native gold as nanoparticle inclusions (e.g., Reich et al. 2005). The gold content of arsenic pyrite is inversely related to its Fe content (Fig. 8e), suggesting that Au substitutes for Fe. A similar conclusion was obtained by Fleet and Mumin (1997), who noted that high concentrations of invisible Au correlate with a deficiency of Fe. Several studies (e.g., Fleet and Mumin 1997; Simon et al. 1999) indicated that the invisible gold in some Carlin-type and VMS deposits is spatially associated with local As enrichment of pyrite grains. The enrichment of pyrite in magmatic trace elements (e.g., As, Au, and Ag) suggests that magmatic fluids contributed to the hydrothermal fluids during sulfide formation (Franklin et al. 2005).

Hydrous fluids in an island-arc setting generally occur at shallow mantle depths and low temperatures (e.g., Hannington et al. 2005), causing a dominance of Zn and enrichment in Ag and Au, which tend to be transported to and to concentrate in low-temperature systems (e.g., Gill et al. 2015). The deposition of sulfide metals is a result of mixing between the exhaled hydrothermal fluids and seawater, leading to a rapid increase in pH and decrease in temperature (Bourcier and Barnes 1987). Hydrous fluids formed Hamama sulfide mineralization caused hydrothermal alteration of the host metavolcanics and provided CO_2 for carbonate formation.

Sphalerite shows a negative correlation between Fe and Zn (Fig. 9a), suggesting a significant Fe substitution at the Zn site in the internal structure of sphalerite (Wright 2009). On the Fe–Cd diagram, sphalerite plots in the overlap between the primary volcanogenic and reformed sphalerite types (Fig. 9b). Galena is Se free, suggesting a low Se content in the ore-forming fluids. The undetectable concentrations of Te in galena and the absence of telluride minerals reflect a low Te content or an absence of Te in the magmatic or hydrothermal fluids that precipitated Hamama deposits (Abd Allah 2012).

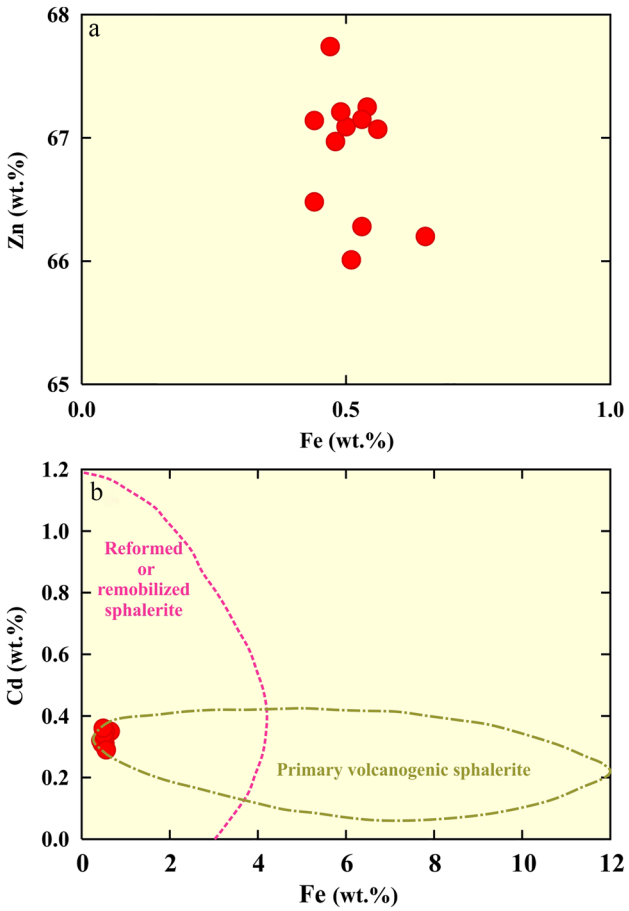

Fig. 9 Sphalerite compositions plotted on **a** Fe–Zn and **b** Fe–Cd discrimination diagrams (Qian 1987)

Conclusions

The main objectives of the present work were achieved by using new field geology, petrography, and mineral chemistry data for sulfide deposits hosted in Hamama metavolcanics and the quartz-carbonate horizon to understand the origin of these deposits and the genetic relationship of these deposits with their host rocks and to explore their tectonic setting and mode of deposition. Also, new trace elements and REEs of Cpx of metabasalts were used to gain information about the mantle source and tectonic setting of these basalts.

The Hamama metavolcanics and their sulfide deposits are the main host of precious metals (e.g., Au, Ag, Zn, and Cu), and the Aton Company recently discovered economic Au in the Hamama gold mine, which then became a promising target for gold exploration in the CED of Egypt. The Hamama metavolcanics are rich in Au and Ag due to several factors that control this mineralization, such as (1) the formation of the host quartz-carbonate exhalite and gossan alteration, (2) the formation of the current VMS deposits in a rift-related setting (a suitable setting for sulfide mineralization) in the Eastern Desert of Egypt, and (3) the dominance of As-rich hydrothermal fluids that allow the accumulation of Au and Ag along shear zones or ancient structural lineaments. This structurally controlled mineralization is supported by the occurrence of NE–SW-trending quartz-feldspar porphyry dikes that intruded metabasalts and the N–S-trending

quartz-specularite vein in the host metavolcanics. In addition, the quartz-carbonate exhalative horizon that hosts the sulfide deposits extends NE–SW along the contact between the metavolcanic and metavolcaniclastic facies. This is considered a channel for hydrothermal circulation and precious metal accumulation, which is enhanced by the effect of the heat engine from late intrusions (e.g., the dacite in the Hamama area).

The Hamama prospect hosts significant Zn–Cu–Ag–Au VMS deposits that represent a typical example of base-metal-type VMS deposits in the ANS. These VMS deposits show a mineralization style that is typical of the bimodal-mafic type. They were possibly formed in a shallow submarine environment in a rifted volcanic-arc setting; in particular, a back-arc basin setting. Sulfide mineralization is hosted in the quartz-carbonate exhalite as semi-massive to massive types and in metabasalt and metadacite as disseminated grains. The VMS deposits are mostly generated from a low-temperature hydrothermal system, as predicted from the enrichment of Zn over Cu and the presence of a low-temperature assemblage (framboidal pyrite, Fe-poor sphalerite, galena, and polybasite). Gold and silver are closely associated with As-bearing pyrite. Silver is also incorporated into the sulfosalt (polybasite). The high concentrations of As, Ag, and Au in the framboidal pyrite suggest that magmatic fluids contributed to the hydrothermal system during sulfide genesis. The As-rich fluids possibly played a vital role in the mobility and accumulation of gold and silver in the Hamama hydrothermal system. Secondary copper deposits were produced by supergene processes in the upper part of the exhalites. Gold and silver are also accumulated in the gossan zone by low-temperature oxidized fluids.

Acknowledgements We would like to express our great appreciation to the Chief Editor Settimio Ferlisi and two anonymous referees for their significant comments and suggestions, which substantially improved the early version of this manuscript.

References

Abd Allah AG (2012) Two genetic types of volcanic-hosted massive sulfide mineralizations from the Eastern Desert of Egypt. Arab J Geosci 5:217–231

Abdel-Karim AM, Ali S, Helmy HM, El-Shafei SA (2016) A fore–arc setting of the Gerf ophiolite, Eastern Desert, Egypt: Evidence from mineral chemistry and geochemistry of ultramafites. Lithos 263:52–65

Abdel-Karim AM, Ali S, El-Shafei SA (2018) Mineral chemistry and geochemistry of ophiolitic metaultramafics from Um Halham and Fawakhir, Central Eastern Desert, Egypt. Int J Earth Sci 107(7):2337–2355. https://doi.org/10.1007/s00531-018-1601-2

Abdel-Karim AM, Ali S, El-Awady A, Elwan W, Khedr MZ, Akihiro T (2019) Mineral and bulk–rock chemistry of Shadli bimodal metavolcanics from Eastern Desert of Egypt: Implication for tectonomagmatic setting and Neoproterozoic continental growth in the Arabian-Nubian Shield. Lithos 338–339:204–217. https://doi.org/10.1016/j.lithos.2019.04.026

Abdel-Karim AM, El-Awady A, Khedr MZ, El-Afandy AH, Elwan W, Tamura T, Ali S (2022) Genesis of sulfide mineralization, Atshan and Darhib Areas, South Eastern Desert of Egypt: evidence of fluid pathway effects along shear zones. Arab J Sci Eng. https://doi.org/10.1007/s13369-021-05736-y

Abdel Nabi A, Aboul Wafa N, El Hawaary MA, Sabet AH (1977) Results of prospecting for gold and rare metals in Wadis Safaga, El Barrud, El Marah and Hamama. Internal report. Geological Survey of Egypt, Cairo, p 24

Abd El-Rahman Y, Surour AA, El-Manawy AW, Rifai M, Abdel Motelib A, Ali WK, El Dougdoug AM (2013) Ancient mining and smelting activities in the Wadi Abu Gerida Area, Central Eastern Desert, Egypt: preliminary results. Archaeometry 55:1067–1087

Abd El-Rahman Y, Surour AA, El-Manawy AW, El-Dougdoug AA, Omar S (2015) Regional setting and characteristics of the Neoproterozoic Wadi Hamama Zn–Cu–Ag–Au prospect: evidence for an intra-oceanic island arc-hosted volcanogenic hydrothermal system. Int J Earth Sci (Geol Rundsch) 104:625–644

Abd El-Rahman Y, Seifert T, Gutzmer J, Said A, Hofmann M, Gärtner A, Linnemann U (2017) The South Um Mongul Cu–Mo–Au prospect in the Eastern Desert of Egypt: from a mid-Cryogenian continental arc to Ediacaran post-collisional appinite-high Ba-Sr monzogranite. Ore Geol Rev 80:250–266. https://doi.org/10.1016/J.OREGEOREV.2016.06.004

Abd El-Rahman Y, Gutzmer J, Li X-H, Seifert T, Chao-Feng Li C-F, Xiao-Xiao Ling X-X, Li J (2020) Not all Neoproterozoic iron formations are glaciogenic: Sturtian-aged non-Rapitan exhalative iron formations from the Arabian-Nubian Shield. Miner Deposita 55:577–596. https://doi.org/10.1007/s00126-019-00898-0

Abdelsalam MG, Stern RJ (1996) Sutures and shear zones in the Arabian-Nubian Shield. J Afr Earth Sci 23:289–310

Akaad MK, El-Ramly MF (1960) Geological history and classification of the basement rocks of the central Eastern Desert of Egypt. Geological Survey of Egypt paper no 9. Geological Survey of Egypt, Cairo

Ali KA, Stern RJ, Manton WI, Kimura JI, Khamis HA (2009) Geochemistry Nd isotopes and U-Pb SHRIMP zircon dating of Neoproterozoic volcanic rocks from the central Eastern Desert of Egypt: new insight into the ~750 Ma crust-forming event. Precambrian Res 171:1–22

Ali KA, Zoheir BA, Stern RJ, Andresen A, Whitehouse MJ, Bishara WW (2016) Lu–Hf and O isotopic compositions on single zircons from the North Eastern Desert of Egypt, Arabian-Nubian Shield: implications for crustal evolution. Gondwana Res 32:181–192

Ali S, Ntaflos T, Sami M (2021) Geochemistry of Khor Um-Safi ophiolitic serpentinites, central Eastern desert, Egypt: implications for neoproterozoic arc-basin system in the Arabian-Nubian shield. Geochemistry 81(1):125690. https://doi.org/10.1016/j.chemer.2020.125690

Ali S, Azer MK, Abdel-Karim AM (2023) Origin and evolution of Neoproterozoic metaophiolitic mantle rocks from the Eastern Desert of Egypt: Implications for tectonic and metamorphic events in the Arabian-Nubian Shield. Geol Acta 21:1–21. https://doi.org/10.1344/GeologicaActa2023.21.6. (**I–VI**)

Al-Shanti AM, El-Mahdy OR, Hassan MA, Hussein AA (1993) A comparative study of five volcanic-hosted sulfide mineralizations in the Arabian Shield. J King Abdulaziz Univ Earth Sci 6:1–33

Aton (2012) Technical report on the Abu Marawat concession, Egypt. https://www.atonresources.com/investor-relations/reports-and-presentations. Accessed 16 Mar 2013

Aton (2017) Hamama west deposit, Abu Marawat concession, Arab Republic of Egypt. https://www.atonresources.com/news/2017/. Accessed 20 June 2017

Azer MK, Farahat ES (2011) Late Neoproterozoic volcano-sedimentary successions of Wadi Rufaiyil, Southern Sinai, Egypt: a case of transition from late-to post-collisional magmatism. J Asia Earth Sci 42:1187–1203

Bailes AH, Galley AG (1999) Evolution of the Paleoproterozoic Snow Lake arc assemblage and geodynamic setting for associated volcanic-hosted massive sulfide deposits, Flin Flon Belt, Manitoba, Canada. Can J Earth Sci 36:1789–1805

Barrie CT, Hannington MD (1999) Classification of volcanic-associated massive sulfide deposits based on host-rock composition. Rev Econ Geol 8:1–11

Barrie CT, Nielsen FW, Aussant CH (2007) The Bisha volcanic-associated massive sulfide deposit, western Nakfa Terrane, Eritrea. Econ Geol 102:717–738

Bence AE, Albee AL (1968) Empirical correction factors for the electron microanalysis of silicate and oxides. J Geol 76:382–403

Bentor YK (1985) The crustal evolution of the Arabo-Nubian Massif with special reference to the Sinai Peninsula. Precambrian Res 28:1–74

Blanchard M, Alfredsson M, Brodholt J, Wright K, Catlow CRA (2007) Arsenic incorporation into FeS_2 pyrite and its influence on dissolution: a DFT study. Geochim Cosmochim Acta 71:624–630

Botros NS (2003) On the relationship between auriferous talc deposits hosted in volcanic rocks and massive sulfide deposits in Egypt. Ore Geol Rev 23:223–257

Bourcier WL, Barnes HL (1987) Ore solution chemistry—VIII. Stabilities of chloride and bisulfide complexes of zinc to 350 °C. Econ Geol 82:1839–1863

Bühler B, Breitkreuz C, Pfänder JA, Hofmann M, Becker S, Linnemann U, Eliwa HA (2014) New insights into the accretion of the Arabian-Nubian Shield: Depositional setting, composition and geochronology of a Mid-Cryogenian arc succession (North Eastern Desert, Egypt). Precambrian Res 243:149–167. https://doi.org/10.1016/j.precamres.2013.12.012

Butler IB, Grimes ST, Rickard D (1999) Iron sulphide oxidation in an anoxic chemostated reaction system. In: Proc 9th VM Goldschmidt Conf, Cambridge, MA, USA, 22–27 Aug 1999, p 45

Callaghan T (2001) Geology and host-rocks alteration of the Henty and Mount Julia gold deposits, Western Tasmania. Econ Geol 96:1073–1088

Cathles LM, Erendi AHJ, Barrie T (1997) How long can a hydrothermal system be sustained by a single intrusive event? Econ Geol 92:766–771

Deditius AP, Reich M, Kesler SE, Utsunomiya S, Chryssoulis SL, Walshe J, Ewing RC (2014) The coupled geochemistry of Au and As in pyrite from hydrothermal ore deposits. Geochim Cosmochim Acta 140:644–670

DeMatties TA (1994) Early Proterozoic volcanogenic massive sulfide deposits in Wisconsin: an overview. Econ Geol 89:1121–1151

Doe BR (1994) Zinc, copper, and lead in mid-ocean ridge basalts and the source rocks control on Zn/Pb in ocean-ridge hydrothermal deposits. Geochim Cosmochim Acta 58:2215–2223

Doyle MG, Allen RL (2003) Subsea-floor replacement in volcanic-hosted massive sulfide deposits. Ore Geol Rev 23:183–222

El-Bialy MZ (2020) Precambrian basement complex of Egypt. In: Hamimi Z, El-Barkooky A, Martínez FJ, Fritz H, Abd El-Rahman Y (eds) The geology of Egypt. Regional geology reviews. Springer, Cham. https://doi.org/10.1007/978-3-030-15265-9_2

El-Gaby S, List FK, Tehrani R (1988) Geology, evolution and metallogenesis of the Pan-African belt in Egypt. In: El-Gaby S, Greiling RO (eds) The Pan-African belt of NE Africa and adjacent areas. Earth evolution sciences. Vieweg and Sohn, Wiesbaden, pp 17–68

El-Gaby S, List FK, Tehrani R (1990) The basement complex of the Eastern Desert and Sinai. In: Said R (ed) The geology of Egypt. Balkema, Rotterdam, pp 175–184

El-Gaby S, Khudeir AA, Abdel Tawab M, Atalla RF (1991) The metamorphosed volcano-sedimentary succession of Wadi Kid, southeastern Sinai, Egypt. Ann Geol Surv Egypt 17:19–35

El-Gaby S (1994) Geologic and tectonic framework of the Pan-African Orogenic belt in Egypt. In: Proc 2nd Int Conf on Geology of the Arab World, Cairo, Egypt, 22–26 Jan 1994, pp 3–17

Farahat ES, Mohamed HA, Ahmed AF, El Mahallawi MM (2007) Origin of I- and A-type granitoids from the Eastern Desert of Egypt: implications for crustal growth in the northern Arabian-Nubian Shield. J Afr Earth Sci 49:43–58

Fleet ME, Mumin AH (1997) Gold-bearing arsenian pyrite and marcasite from Carlin Trend deposits and laboratory synthesis. Am Mineral 82:182–193

Fowler A, Ali KG, Omar SM, Eliwa H (2006) The significance of gneissic rocks and synmagmatic extensional ductile shear zones of the Barud area for the tectonics of the North Eastern Desert, Egypt. J Afr Earth Sci 46:201–220

Franklin JM, Gibson HL, Jonasson IR, Galley AG (2005) Volcanogenic massive sulphide deposits. In: Hedenquist JW, Thompson JFH, Goldfarb RJ, Richards JP (eds) Economic geology (100th anniversary volume). The Economic Geology Publishing Company, Lancaster, pp 523–560

Fritz H, Abdelsalam M, Ali KA, Bingen B, Collins AS, Fowler AR, Hauzenberger CA, Johnson PR, Kusky TM, Macey P, Muhongo S, Ghebreab W, Stern RJ, Viola G (2013) Orogen styles in the East African Orogen: a review of the Neoproterozoic to Cambrian tectonic evolution. J Afr Earth Sci 86:65–106

Galley AG (2003) Composite synvolcanic intrusions associated with Precambrian VMS-related hydrothermal systems. Miner Deposita 38:443–473

Galley AG, Hannington M, Jonasson I (2007) Volcanogenic massive sulphide deposits. In: Goodfellow WD (ed) Mineral deposits of Canada: a synthesis of major deposit types, district metallogeny, the evolution of geological provinces, and exploration methods. Special Publication 5. Mineral Deposits Division, Geological Association of Canada, St. John's, pp 141–161

Gamal El Dien H, Li Z-X, Abu Anbar M, Doucet LS, Murphy JB, Evans NJ, Xia X-P, Li J (2021) Two-stage crustal growth in the Arabian-Nubian shield: initial arc accretion followed by plume-induced crustal reworking. Precambrian Res 359:106211

Gemmell JB, Fulton R (2001) Geology, genesis, and exploration implications of the footwall and hanging-wall alteration associated with the Hellyer volcanic-hosted massive sulfide deposit, Tasmania, Australia. Econ Geol 96:003–1035

Gill SB, Piercey SJ, Layton-Mattews D, Layne GD, Piercey G (2015) Mineralogical, sulphur, and lead isotopic study of the Lemarchant Zn-Pb-Cu-Ag-Au-VMS deposit: implications for precious-metal enrichment processes in the VMS environment. In: Peter JM, Mercier-Langevin P (eds) Targeted Geoscience Initiative 4: contributions to the understanding of volcanogenic massive sulphide deposit genesis and exploration methods development. Open File 7853. Geological Survey of Canada, Ottawa, pp 183–95

Halley SW, Roberts RH (1997) Henty: a shallow-water gold-rich volcanogenic massive sulfide deposit in Western Tasmania. Econ Geol 92:438–447

Hannington MD, Jonasson IR, Herzig PM, Petersen S (1995) Physical and chemical processes of seafloor mineralization at midocean ridges. In: Humphris SE, Zierenberg RA, Mullineaux LS, Thomson RE (eds) Seafloor hydrothermal systems: physical, chemical, biological and geological interactions: Geophysical Monograph 91. American Geophysical Union, pp 115–157

Hannington M (2014) Volcanogenic massive sulfide deposits. In: Scott SD (ed) Treatise on geochemistry, vol 13, 2nd edn. Elsevier-Pergamon, Oxford, pp 463–488

Hannington MD, Bleeker W, Kjarsgaard IM (1999) Sulphide mineralogy, geochemistry and ore genesis of the Kidd Creek deposit: part II. The bornite zone. Econ Geol Monogr 10:225–266

Hannington MD, Santaguida F, Kjarsgaard IM, Cathles LM (2003) Regional greenschist facies hydrothermal alteration in the central Blake River Group, western Abitibi subprovince, Canada. Miner Deposita 38:393–422

Hannington MD, De Ronde CEJ, Petersen S (2005) Sea-floor tectonics and submarine hydrothermal systems. In: Hedenquist JW, Thompson JFH, Goldfarb RJ, Richards JP (eds) 100th anniversary volume of economic geology. Society of Economic Geologists, Littleton, pp 111–142

Harbi HM, Surour AA, Davidson GJ (2014) Genesis of Neoproterozoic Au-bearing volcanogenic sulfides and quartz veins in the Ar Rjum goldfield, Saudi Arabia. Ore Geol Rev 58:110–125

Hart SR, Dunn T (1993) Experimental cpx/melt partitioning of 24 trace elements. Contrib Mineral Petrol 113:1–8

Hart TR, Gibson HL, Lesher CM (2004) Trace element geochemistry and petrogenesis of felsic volcanic rocks associated with volcanogenic massive Cu–Zn–Pb sulfide deposits. Econ Geol 99:1003–1013

Hassan YM (2005) Geology and mineralization of the Precambrian rocks at Wadi Hamama area, central Eastern Desert. MSc dissertation. Cairo University, Cairo

Hassan MA, Hashad AH (1990) Precambrian of Egypt. In: Said R (ed) The geology of Egypt. Balkema, Rotterdam, pp 201–248

Helmy HM (1999) The Um Samiuki volcanogenic Zn–Cu–Pb–Ag deposit, Eastern desert, Egypt: a possible new occurrence of Cervelleite. Can Mineral 37:143–158

Herzig PM, Hannington MD (1995) Polymetallic massive sulfides at modern seafloor. Ore Geol Rev 10:95–115

Huston DL, Taylor T, Fabray J, Patterson DJ (1992) A comparison of the geology and mineralization of the Balcooma and Dry River South volcanic-hosted massive sulfide deposits, Northern Queensland. Econ Geol 87:785–811

Huston DL, Pehrsson S, Eglington BM, Zaw K (2010) The geology and metallogeny of volcanic-hosted massive sulfide deposits: variations through geologic time and with tectonic setting. Econ Geol 105:571–591

Inverno CMC, Solomon M, Barton MD, Foden J (2008) The Cu stockwork and massive sulfide ore of the Feitais volcanic-hosted massive sulfide deposit, Aljustrel, Iberian Pyrite Belt, Portugal: a mineralogical, fluid inclusion, and isotopic investigation. Econ Geol 103:241–267

Johnson KTM (1998) Experimental determination of partition coefficients for rare earth and high field strength elements between clinopyroxene, garnet and basaltic melt. Contrib Mineral Petrol 133:60–68

Johnson PR, Andresen A, Collins AS, Fowler AR, Fritz H, Ghebreab W, Kusky T, Stern RJ (2011) Late Cryogenian-Ediacaran history of the Arabian-Nubian Shield: a review of depositional, plutonic, structural, and tectonic events in the closing stages of the northern East African Orogen. J Afr Earth Sci 61:67–232

Kamal El-Din G, Abdelkareem M (2018) Integration of remote sensing, geochemical and field data in the Qena-Safaga shear zone: implications for structural evolution of the Eastern Desert, Egypt. J Afr Earth Sci 141:179–193

Khedr MZ, El-Awady A, Arai S, Hauzenberger C, Tamura A, Stern RJ, Morishita T (2020) Petrogenesis of the ~740 Korab Kansi mafic-ultramafic intrusion, South Eastern Desert of Egypt: evidence of Ti-rich ferropicritic magmatism. Gondwana Res 82:48–72

Khedr MZ, Al Desouky AA, Takazawa E, Kamh S, Hauzenberger C, Whattam SA, El-Awady A (2023) Remote sensing and geochemical investigations of sulfide-bearing metavolcanic and gabbroic rocks (Egypt): constraints on host-rock petrogenesis and sulfide genesis. Gondwana Res 119:282–312

Koski RA (2012) Supergene ore and gangue characteristics in volcanogenic massive sulfide occurrence model. US Geological Survey Scientific Investigation Report 2010-5070-C. US Geological Survey, Reson, Chap 12

Kröner A, Todt W, Hussein IM, Mansour M, Rashwan AA (1992) Dating of late Proterozoic ophiolites in Egypt and the Sudan using the single grain zircon evaporation technique. Precambrian Res 59:15–32. https://doi.org/10.1016/0301-9268(92)90049-T

Kröner A, Krüger J, Rashwan AAA (1994) Age and tectonic setting of granitoid gneisses in the Eastern Desert of Egypt and South-West Sinai. Geol Rundsch 83:502–513

Large RR (1992) Australian volcanic-hosted massive sulfide deposits: features, styles, and genetic models. Econ Geol 87:471–510

Large RR, Both RA (1980) The volcanogenic sulfide ores at Mount Chalmers, Eastern Queensland. Econ Geol 75:992–1009

Large RR, Doyle M, Raymond O, Cooke D, Jones A, Heasman L (1996) Evaluation of the role of Cambrian granites in the genesis of world class VHMS deposits in Tasmania. Ore Geol Rev 10:215–230

Leeman WP (1996) Boron and other fluid-mobile elements in volcanic arc lavas: Implications for subduction processes. In: Bebout GE, Scholl DW, Kirby SH, Platt JP (eds) Subduction: top to bottom. American Geophysical Union, Washington, DC, pp 269–276

Liaghat S, MacLean WH (1992) The Key Tuffite, Matagami mining district: origin of tuff components and mass changes. Explor Min Geol 1:197–207

McDonough WF, Sun SS (1995) The composition of the Earth. Chem Geol 120:223–253

Minex Mineral Egypt (1991) Report on exploration percussion drilling at Hamama (b). Internal Report of the Geological Survey of Egypt 9(b). Geological Survey of Egypt, Cairo

Moghazi AM (2003) Geochemistry and petrogenesis of a high-K calc–alkaline Dokhan volcanic suite, South Safaga area, Egypt: the role of late Neoproterozoic crustal extension. Precambrian Res 423:161–178

Mohamed HA, Ali S, Sedki T, Abdelkhalik I (2019) The Sukari Neoproterozoic granitoids, Eastern Desert, Egypt: petrological and structural implications. Afr Earth Sci 149:426–440. https://doi.org/10.1016/j.jafrearsci.2018.08.020

Morishita T, Ishida Y, Arai S, Shirasaka M (2005) Determination of multiple trace element compositions in thin (b30 μm) layers of NIST SRM 614 and 616 using laser ablation–inductively coupled plasma-mass spectrometry. Geostand Geoanal Res 29:107–122

Norman M, Garcia MO, Pietruszka A (2005) Trace-element distribution coefficients for pyroxenes, plagioclase, and olivine in evolved tholeiites from the 1955 eruption of Kilauea Volcano, Hawai'i, and petrogenesis of differentiated rift-zone lavas. Am Miner 90:888–899

Ohmoto H (1996) Formation of volcanogenic massive sulphide deposits: the Kuroko perspective. Ore Geol Rev 10:135–177

Ohmoto H, Mizukami M, Drummond SE, Eldridge CS, Pisutha-Arnond V, Lenagh T (1983) Chemical processes of Kuroko formation. Econ Geol Monogr 5:570–604

Pearce NJG, Perkins WT, Westgate JA, Gorton MP, Jackson SE, Neal CR, Chenery SP (1997) A compilation of new and published major and trace element data for NIST SRM 610 and NIST SRM 612 glass reference materials. Geostand Newsl J Geostand Geoanal 21:115–144

Peter JM, Goodfellow WD (1996) Mineralogy, bulk and rare earth element geochemistry of massive sulfide-associated hydrothermal sediments of the Brunswick Horizon, Bathurst Mining Camp, New Brunswick. Can J Earth Sci 33:252–283

Petersen S, Herzig PM, Hannington MD (2000) Third dimension of a presently forming VMS deposit: TAG hydrothermal mound, Mid-Atlantic Ridge, 26°N. Miner Depos 35:233–259

Pierce SJ (2011) The setting, style, and role of magmatism in the formation of volcanogenic massive sulfide deposits. Miner Deposita 46:449–471

Piercey SJ, Squires GC, Brace TD (2014) Lithostratigraphic, hydrothermal, and tectonic setting of the Boundary volcanogenic massive sulfide deposit, Newfoundland Appalachian, Canada: formation by subseafloor replacement in a Cambrian rifted arc. Econ Geol 109:661–687

Poulsen H, Hannington M (1995) Auriferous volcanogenic sulfide deposits. In: Eckstrand OR, Sinclair WD, Thorpe RI (eds) Geology of Canadian mineral deposit types. Geology of Canada no. 8. Geological Survey of Canada, Ottawa, 1:183–196

Qian Z (1987) Trace elements in galena and sphalerite and their geochemical significance in distinguishing the genetic types of Pb-Zn ore deposits. Chin J Geochem 6:177–190

Reich M, Kesler SE, Utsunomiya S, Palenik CS, Chryssoulis SL, Ewing RC (2005) Solubility of gold in arsenian pyrite. Geochim Cosmochim Acta 69:2781–2796

Riverin G, Hodgson CJ (1980) Wall-rock alteration at the Millenbach Cu–Zn Mine, Noranda, Quebec. Econ Geol 75:424–444

Saha A, Mudholkar AV, Raju KAK, Doley B, Sensarma S (2019) Geochemical characteristics of basalts from Andaman subduction zone: Implications on magma genesis at intraoceanic back-arc spreading centres. Geol J 54(6):3489–3508. https://doi.org/10.1002/gj.3345

Sami M, Adam MMA, Lv X, Lasheen ESR, Ene A, Zakaly HMH, Alarifi SS, Mahdy NM, Abdel Rahman ARA, Saeed A, Farahat ES, Fathy D, Ali S (2023) Petrogenesis and tectonic implications of the cryogenian I-type granodiorites from Gabgaba Terrane (NE Sudan). Minerals 13(3):331. https://doi.org/10.3390/min13030331

Santaguida F, Gibson HL, Watkinson DH, Hannington MD (1998) Semi-conformable epidote-quartz hydrothermal alteration in the Central Noranda Volcanic complex: relationship to volcanic activity and VMS mineralization. In: Bailes AH, Galley AG, Hannington MD, Holk G, Katsube J, Paquette F, Paradis S, Santaguida F, Taylor B (eds) The use of regional-scale alteration and subvolcanic intrusions in the exploration for volcanic-associated massive sulphide deposits. Annual report. Canadian Minerals Research Organization Project 94E07. CAMIRO Exploration Division, Toronto, pp 139–180

Shalaby IM, Stumpfl E, Helmy HM, El Mahallawi MM, Kamel OA (2004) Silver and silver-bearing minerals at the Um Samiuki volcanogenic massive sulfide deposit, Eastern Desert, Egypt. Miner Depos 39:608–621

Shukri NM, Mansour MS (1980) Lithostratigraphy of Um Samiuki district, Eastern Desert, Egypt, vol 4. Institute of Applied Geology, Jeddah University, Jeddah, pp 83–93

Simon G, Kesler SE, Chryssoulis S (1999) Geochemistry and textures of gold-bearing arsenian pyrite, Twin Creeks, Nevada: implications for deposit ion of gold in Carlin-type deposits. Econ Geol 94:405–421

Singer DA (1995) World class base and precious metal deposits; a quantitative analysis. Econ Geol 90:88–104

Stern RJ (1994) Arc assembly and continental collision in the Neoproterozoic East African Orogen: implications for the consolidation of Gondwana land. Ann Rev Earth Planet Sci 22:319–351

Stern RJ (2002) Crustal evolution in the East African Orogen: a neodymium isotopic perspective. J Afr Earth Sci 34:109–117

Stern RJ, Hedge C (1985) Geochronologic and isotopic constraints on late Precambrian crustal evolution in the Eastern Desert of Egypt. Am J Sci 285:97–127

Stern RJ, Kröner A, Rashwan AA (1991) A Late Precambrian (~710Ma) high vulcanicity rift in the south Eastern Desert of Egypt. Int J Earth Sci 80:155–170

Stosch H-G (1982) Rare earth partitioning between minerals from anhydrous spinel peridotite xenoliths. Geochim Cosmochim Acta 46:793–811

Surour A, Bakhsh R (2013) Microfabrics and microchemistry of sulfide ores from the 640 FEW level at the Al Amar gold mine, Saudi Arabia. J Microsc Ultrastruct 1:96–110

Takla MA, Suror AA, El-Mansi MM (1998) Microfabrics and mineral chemistry of sulphides from Shadli metavolcanics and younger gabbros, Eastern Desert, Egypt. Anna Geol Surv Egypt XXI:191–215

Tauson VL (1999) Gold solubility in the common gold-bearing minerals: experimental evaluation and application to pyrite. Eur J Mineral 11:937–947

Whalen JB, McNicoll VJ, Galley AG, Longstaffe FJ (2004) Tectonic and metallogenic importance of an Archean composite high- and low-Al tonalite suite, Western Superior Province, Canada. Precambrian Res 132:275–301

Wright K (2009) The incorporation of cadmium, manganese and ferrous iron in sphalerite: insights from computer simulations. Can Mineral 47:615–623